Titre: Title: Actuating Metamaterials via Centrifugal Force: Towards Passively Adapting Permanent Magnet Synchronous Motors

Auteur: Author: Étienne Leclerc

Date: 2026

Type: Mémoire ou thèse / Dissertation or Thesis

Référence: Citation: Leclerc, É. (2026). Actuating Metamaterials via Centrifugal Force: Towards Passively Adapting Permanent Magnet Synchronous Motors [Master's thesis, Polytechnique Montréal]. PolyPublie. https://publications.polymtl.ca/76504/

Directeurs de recherche: Advisors: David Mélançon

Programme: Program: Génie mécanique

POLYTECHNIQUE MONTRÉAL
affiliée à l'Université de Montréal

Actuating Metamaterials via Centrifugal Force: Towards Passively Adapting Permanent Magnet Synchronous Motors

ÉTIENNE LECLERC
Département de génie mécanique

Mémoire présenté en vue de l'obtention du diplôme de *Maîtrise ès sciences appliquées*
Génie mécanique

Mai 2026

POLYTECHNIQUE MONTRÉAL
affiliée à l'Université de Montréal

Ce mémoire intitulé :

Actuating Metamaterials via Centrifugal Force: Towards Passively Adapting Permanent Magnet Synchronous Motors

présenté par **Étienne LECLERC**
en vue de l'obtention du diplôme de *Maîtrise ès sciences appliquées*
a été dûment accepté par le jury d'examen constitué de :

Aurelian VADEAN, président
David MÉLANÇON, membre et directeur de recherche
Fabrice BERNIER, membre

RÉSUMÉ

Les matériaux d'ingénierie conventionnels sont limités par leurs propriétés intrinsèques, telles que le module de Young et la densité, ce qui restreint les possibilités de conception. Les métamatériaux permettent de surmonter ces limites en exploitant la géométrie pour définir le comportement structural plutôt que de dépendre seulement de la composition du matériau. Des comportements uniques, tels que la raideur négative et la multistabilité, permettent d'obtenir des réponses à des stimuli externes pouvant être adaptées à différentes applications, comme l'absorption d'énergie ou l'isolation acoustique. Ce mémoire présente un méta-disque composé de cellules élémentaires à symétrie cyclique, qui change de configuration de manière passive selon la vitesse de rotation. Chaque cellule est programmée pour se déformer sous l'effet de la force centrifuge. La conception proposée comprend deux parties : une base intégrant un treillis de von Mises, dont la réponse peut être ajustée en modifiant ses paramètres géométriques afin d'obtenir un contrôle précis de la déformation sous rotation; et une masse supérieure ajoutant de l'inertie, permettant ainsi la déformation à haute vitesse.

Le comportement de la structure sous chargement centrifuge est caractérisé à l'aide de simulations par éléments finis. Nous démontrons que quatre types de réponses peuvent être obtenus: (1) non linéaire, (2) transitoire, (3) à saut et (4) bistable. Nous construisons un espace de conception du comportement statique force-déplacement en faisant varier les paramètres géométriques, et nous exploitons cet espace pour démontrer la programmabilité de la cellule et prédire sa réponse centrifuge sans recourir à des simulations supplémentaires. Afin de valider les résultats numériques, des échantillons de la cellule sont moulés en silicone (Smooth-Sil 960), et leur réponse mécanique est mesurée sous déplacement imposé ainsi que sous force centrifuge à l'aide d'un banc d'essai développé.

Enfin, nous montrons que le déplacement de la cellule peut être programmé et contrôlé en fonction de la vitesse de rotation afin de répondre aux exigences de diverses applications. En collaboration avec le Conseil national de recherches du Canada (CNRC), nous démontrons l'applicabilité du concept aux moteurs synchrones à aimants permanents (PMSM) pour réaliser un affaiblissement du flux de manière mécanique, améliorant ainsi la performance à haute vitesse d'un moteur de Toyota Prius. Les simulations montrent que ce concept permet au moteur de maintenir son couple au-delà de 10 000 tr/min. Cette preuve de concept permet de poser les bases des futurs méta-moteurs à grande vitesse pour l'aérospatiale, capables de dépasser 30 000 tr/min.

ABSTRACT

Conventional engineering materials are limited by intrinsic properties such as Young's modulus and density, constraining design flexibility. Metamaterials overcome these limitations by leveraging geometry to define structural behavior rather than relying solely on material composition. Unique behaviors such as negative stiffness and multistability enable responses to external stimuli that can be tailored to specific applications, like energy absorption or acoustic isolation. This thesis presents a meta-disk composed of cyclically repeated unit cells that passively changes shape based on rotational speed. Each unit cell is programmed to deform under the effect of centrifugal force. The proposed design consists of two parts: a base featuring a von Mises truss, whose response can be tuned by varying truss parameters (e.g., thickness and slope) to achieve precise displacement control under rotation; and a top mass that provides inertia, thereby enabling deformation at high speeds.

The behavior of the structure under centrifugal loading is characterized using finite element simulations. We demonstrate that four response types can be achieved: (1) non-linear, (2) transient, (3) snap-through, and (4) bistable. We create a design space of the static force-displacement response by varying geometric parameters, and we exploit this design space to demonstrate programmability and to predict the structure's centrifugal response without additional simulations. To validate the simulation results, unit cell samples are molded in silicone (Smooth-Sil 960), and their mechanical response is measured both under imposed displacement and under centrifugal force using a custom-developed test rig.

Finally, we show that the displacement of the unit cell can be programmed and controlled as a function of rotational speed to match diverse application requirements. In collaboration with the National Research Council of Canada (NRC), we demonstrate the applicability of the concept to Permanent Magnet Synchronous Motors (PMSMs) for mechanical flux weakening, improving high-speed performance without increasing system complexity or cost of a Toyota Prius motor equipped with the proposed design. Simulations showed that such design enables the motor to maintain torque beyond 10 000 rpm. This proof of concept lays the foundation for future high-speed meta-motors for aerospace applications, where motors need to exceed 30 000 rpm.

TABLE OF CONTENTS

LIST OF TABLES

LIST OF FIGURES

LIST OF SYMBOLS AND ACRONYMS

Acronyms

PMSM	Permanent Magnet Synchronous Motor
IPMSM	Interior Permanent Magnet Synchronous Motor
PM	Permanent magnet
NRC	National Research Council of Canada
FE	Finite Element
3D	Three-dimensional
2D	Two-dimensional
FFF	Fused Filament Fabrication
DIW	Direct Ink Writing
LPBF	Laser Powder Bed Fusion
RPM	Rotation Per Minute
DC	Direct Current
AC	Alternating Current
RF	Reaction Force
PLA	PolyLactic Acid
TPU	ThermoPlastic Polyurethane
FPS	Frame Per Second
EMF	Electromagnetic Force

Symbols

T	Torque
u_s	stator voltage
λ_{pm}	flux linkage
i	current
ω	Angular rotation speed
$(\cdot)_{max}$	Used to refer to maximum value
δ	Displacement
δ^*	Displacement normalized by a
l	Width of the von Mises truss
a	Slope of the von Mises truss
t_s	Thickness of the von Mises truss

t_w	Thickness of the beam connecting the von Mises truss to the block
h_b	Height of the block
t_{gap}	Space between the block and the von Mises truss
r	Distance from the center of the meta-disk
d	Depth of the structure

LIST OF APPENDICES

CHAPTER 1 INTRODUCTION

Unlike conventional engineering materials, mechanical metamaterials can be engineered to exhibit unique behaviors through their structure rather than their material composition. These properties include auxetic behavior such as shape morphing [1], negative stiffness [2], and multistability [3]. Mechanical metamaterials can be actuated through various stimuli, such as displacement or force [4], pressure [5], temperature [6], or centrifugal force [7] to enable novel applications in mechanical and aerospace engineering.

In particular, harnessing centrifugal force in metamaterials could provide a simple way of achieving passive reconfiguration in rotating machines. In this context, reconfiguration refers to a deformation that leads to a shape change in the geometry of the structure using elastic deformation, for example by altering inertia in flywheels [8] or implementing flux-weakening techniques in electric motors, particularly Permanent Magnet Synchronous Motors (PMSMs). In industry, PMSMs are among the most commonly used electric motors due to their high power density and efficiency [9]. However, one of their limitations is the inability to deliver continuous maximum power at high speeds, as torque decreases beyond a certain rotor speed [10]. To mitigate this issue, flux-weakening techniques have been developed, allowing these motors to operate at maximum power over a broader speed range [11]. These techniques are typically implemented algorithmically, which increases system complexity and cost [12].

This thesis proposes a modular centrifugal force-driven meta-disk capable of exhibiting a large deformation under rotation. Using finite element (FE) simulations, we characterize the static and dynamic behavior of the meta-disk. Experimental testing is then used to validate these results under static and dynamic loading. Finally, we demonstrate that the meta-disk deformation can be programmed as a function of rotation. In collaboration with the National Research Council of Canada (NRC), we apply our design to induce a mechanical flux weakening, with simulations confirming improved performance in a Toyota Prius motor.

This thesis is organized as follows. Chapter 2 presents a literature review on metamaterials, electric motors, and flux-weakening techniques. Chapter 3 defines the objectives of the thesis. Chapter 4 details the proposed geometry, simulations, parameterization, and optimization process. Chapter 5 provides experimental validation of the simulation results. Chapter 6 demonstrates that the meta-disk displacement can be programmed under rotational loading and explores its potential use as a passive solution for performance optimization in PMSMs. Finally, the Conclusion and Outlook summarize the results, propose improvements, and suggest future research directions.

CHAPTER 2 LITERATURE REVIEW

2.1 Classification of engineering materials

Mechanical performance is traditionally associated with the chemical composition of a material, but recent studies [13–15] have shown that geometry can be used to program the mechanical response. Materials can be broadly classified in three categories based on how their mechanical properties arise: monolithic materials, architected materials, and metamaterials. Figure 2.1 shows a comparative overview of these categories and highlights how geometry can be used to control mechanical performance. Monolithic materials, pictured in Figure 2.1A, represent conventional solid materials, such as bulk metals like aluminium. Those materials have their mechanical properties, e.g., Young's modulus and yield strength, that are defined solely by their chemical composition [16]. Architected materials, shown in Figure 2.1B, are made of a lattice network whose topology and relative density can be designed to achieve target mechanical properties. This allows the creation of structures with high specific properties and mechanical behavior programmed based on the intended application [17, 18]. Mechanical metamaterials extend this control and flexibility even further by exploiting nonlinear geometry effects such as buckling and snapping as well as large displacements and rotations. As illustrated in Figure 2.1C, their mechanical properties are primarily defined by the geometry of a repeated unit cell [19, 20].

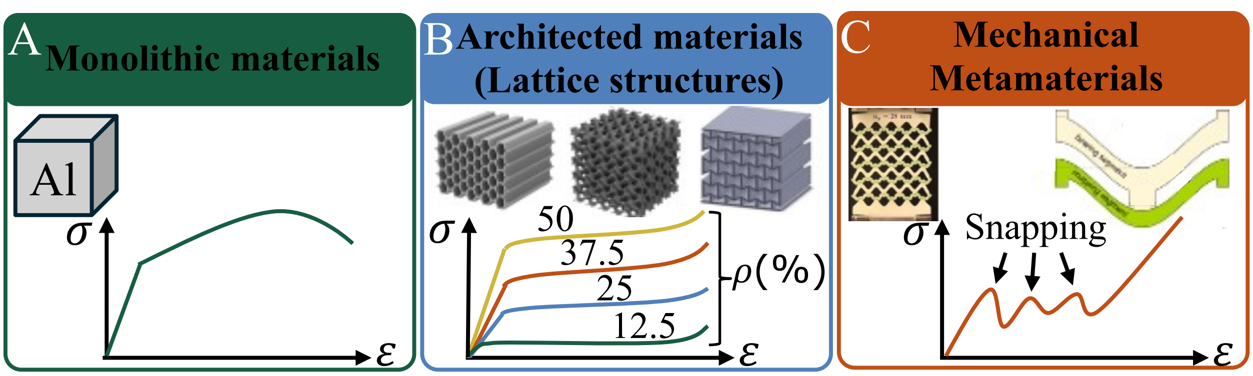

Figure 2.1 | **Classification of engineering metamaterials. (A)** Monolithic materials, like metals or foams, exhibit uniform properties determined solely by their chemical composition [16] **(B)** Architected materials, like lattice structures, allow tuning of mechanical properties (e.g. stiffness, strength) by varying their topology or relative density ρ [21] **(C)** Metamaterials are advanced architectures whose properties are defined by their geometry, enabling application-specific functionalities such as nonlinear or programmable responses [20] **Legend:** Stress–strain (σ–ϵ) curves for each category

2.2 Properties of metamaterials

Figure 2.2 illustrates some of the exotic properties and functionalities achievable in mechanical metamaterials. For instance, cutting a specific pattern into a flat sheet material has been used to achieve shape morphing structures that deform into predetermined three-dimensional (3D) shapes [1] (see Figure 2.2A). Geometric frustration in an elastic beam can be exploited to generate negative stiffness which can be used to have snap-through structures. [22] (see Figure 2.2B). Origami-inspired configurations enable structures with multiple stable states, enabling structures to remain in a configuration once deformed [3, 23] (see Figure 2.2C). Additionally, complex geometric architectures can be designed to create a structure exhibiting a negative Poisson's ratio, defined as an auxetic behavior [24, 25] (see Figure 2.2D). Furthermore, by coupling two von Mises trusses, the effective stiffness of a structure can be designed to switch from a softer to a stiffer state [26, 27] (see Figure 2.2E).

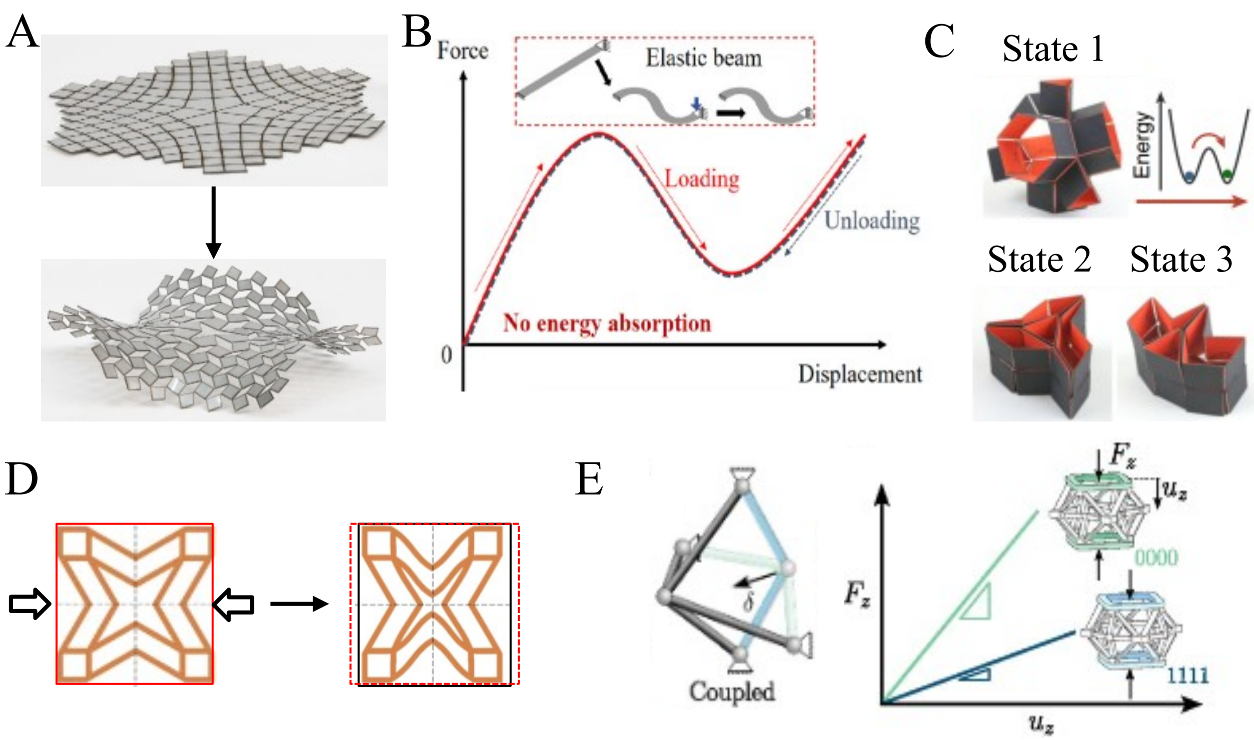

Figure 2.2 | **Properties of metamaterials.** **(A)** A flat sheet with patterned cuts that morphs into a predetermined 3D shape [1] **(B)** Force-displacement response of an elastic beam attached on one side displaying negative stiffness [22] **(C)** Origami-inspired structure with multiple stable configurations [3] **(D)** Deformation of a structure with a negative Poisson's ratio [24] **(E)** Programmable stiffness achieved by coupling two von Mises trusses [26]

2.3 Lattice-based mechanical metamaterials

The thesis focuses on lattice-based mechanical metamaterials, i.e., structures made of truss-like members. Figure 2.3 presents classical lattice-based geometries from the literature. One of them is the von Mises truss, composed of a single beam pinned at both ends. Under a force, the beam snaps and transitions to a mirror position relative to its initial position [28](see Figure 2.3A). The unit cell can be modified by coupling two von Mises trusses connected at their center, enabling multistable structures [4, 26](see Figure 2.3B). Another classical architecture is the "scissor-lift", composed of two elastic beams connected to each other by the side that produces large deformation [29] (see Figure 2.3C). Lastly, a unit cell made of re-entrant hexagon exhibits auxetic behavior [30, 31] (see Figure 2.3D).

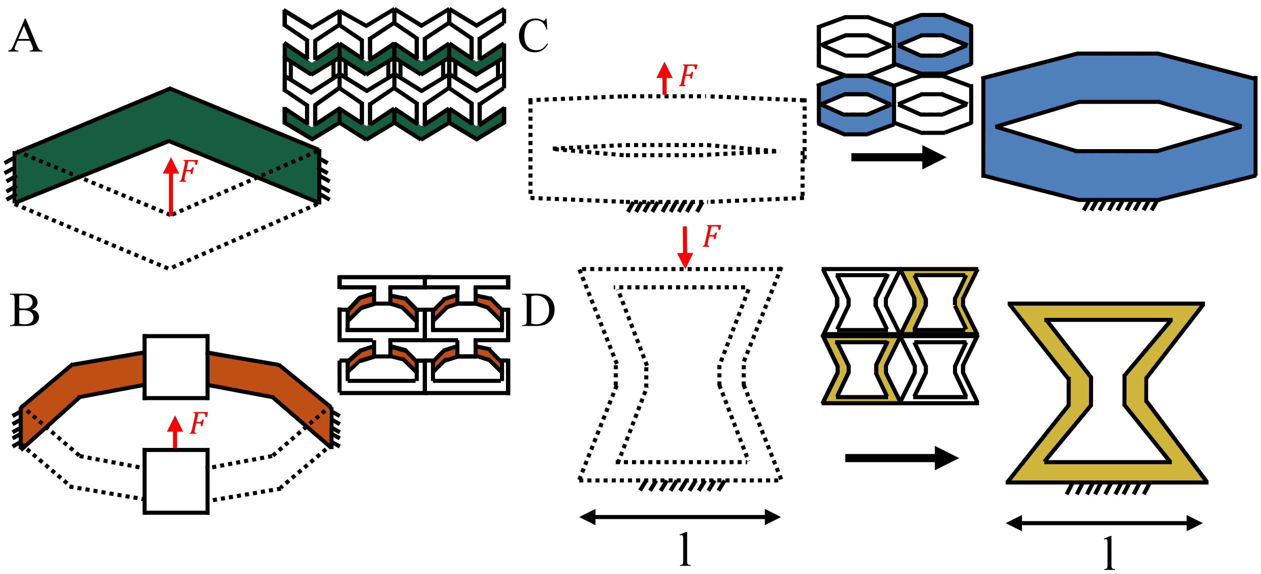

Figure 2.3 | **Lattice-based mechanical metamaterials.** Classical unit cell geometries **(A)** Von Mises truss **(B)** Double von Mises trusses **(C)** Scissor lift **(D)** Re-entrant hexagon **Legend:** Undeformed (dashed lines) and deformed (solid lines) configurations are shown

2.4 Fabrication of lattice-based mechanical metamaterials

Lattice-based mechanical metamaterials can be fabricated using various processes at different scales, each offering different trade-offs. Figure 2.4 presents several techniques commonly reported in the literature, highlighting some of the benefits and drawbacks of each fabrication method. Laser cutting enables the rapid creation of complex 3D geometries from flat sheets. However, because it is a two-dimensional (2D) fabrication process, achieving 3D forms requires carefully designed patterns and folding strategies [32] (see Figure 2.4A).

Cast molding is a commonly used fabrication method in metamaterial research [33]. It is frequently employed with elastomers as it provides an easy way to create highly deformable, elastic structures. Its main limitations are the need for mold fabrication and curing times that can range from several minutes to multiple hours, depending on the material [4] (see Figure 2.4B). Additive manufacturing is another fabrication process to realize mechanical metamaterials [33]. For instance, Fused Filament Fabrication (FFF) have become more popular with the growing accessibility and speed of 3D printers. However, a major drawback of this process is the anisotropy of the parts, as their mechanical properties depend on the printing orientation which can lead to failure under specific loading conditions [34] (see Figure 2.4C). Lastly, another extrusion-based fabrication process is Direct Ink Writing (DIW). This method can print extremely small and precise structures, and carbon fibers can be incorporated into the ink to produce structures with high mechanical properties [35] (see Figure 2.4D).

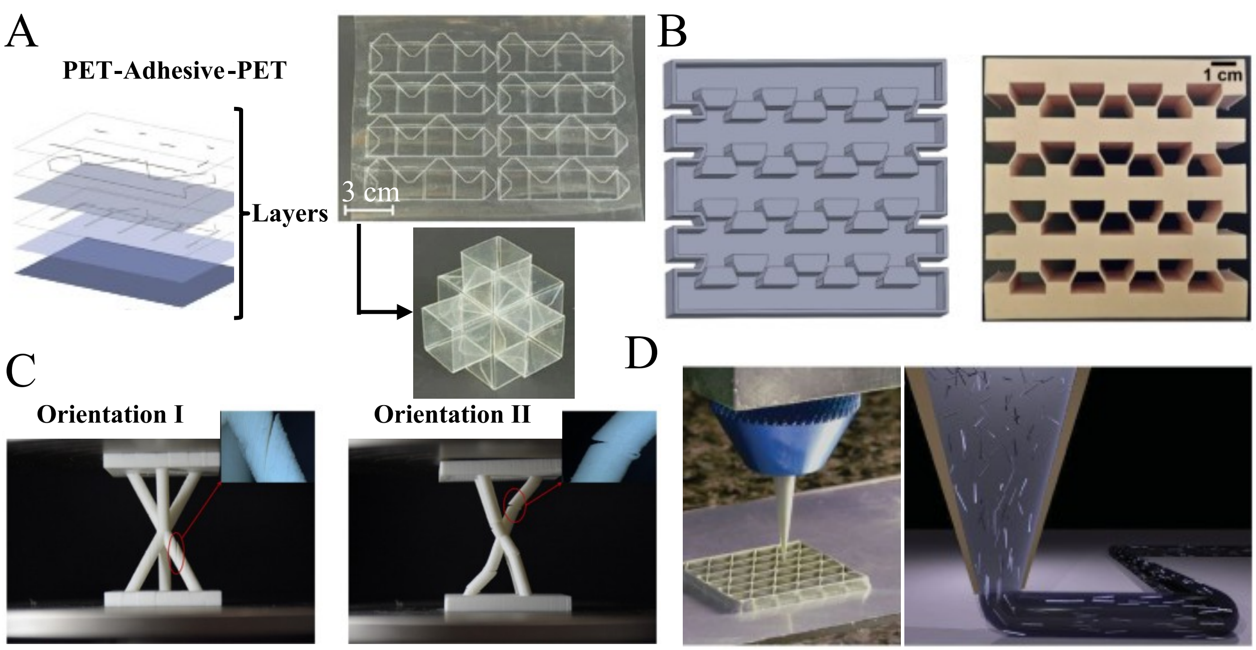

Figure 2.4 | **Fabrication of lattice-based mechanical metamaterials. (A)** Fabrication of a structure with multiple degrees of freedom using laser cutting [32] **(B)** Molding of a deformable metamaterial structure [4] **(C)** Kagome lattice structures fabricated using Fused Filament Fabrication (FFF) [34] **(D)** Fabrication of lightweight, carbon fiber-reinforced honeycomb lattice using Direct Ink Writing (DIW) [35]

2.5 Actuation of lattice-based mechanical metamaterials

Lattice-based mechanical metamaterials can be actuated through various external stimuli, as illustrated in Figure 2.5. The most common approach is to apply a mechanical force, such as compression, to deform the structure [4] (see Figure 2.5A). Several non-contact actuation methods have also been demonstrated. For instance, a lattice structure can open under the application of an external magnetic field [36] (see Figure 2.5B). Another approach consists of applying air pressure to induce buckling in thin-walled tubes [37] (see Figure 2.5C). Buckling can also be induced by centrifugal loading when the structure rotates at high speed [7] (see Figure 2.5D). The same authors also demonstrated a precise control over the buckling of a structure subjected to centrifugal forces by developing a rotating disk with memory capabilities. In their design, bistable beams on the rotating platform are configured to switch states at specific rotational speed thresholds, storing mechanically the information using the angular velocity and acceleration of the platform [38]. Finally, metamaterials can be deformed through heating by using materials like shape memory alloys that are responsive to temperature variations (see Figure 2.5E) [39].

2.6 Engineering applications of mechanical metamaterials

While traditional engineering systems rely on mechanical elements such as springs, gears, or hinges, recent studies in mechanical metamaterials have shown that large and controlled deformations can be programmed directly into the unit cell geometry [41]. Because their deformation is triggered solely by the applied stimulus, without the need for sensors, motors, or electronic control, these structures can operate entirely passively. By exploiting the metamaterial properties like variable stiffness, nonlinear deformation or multistability, these structure behaviors can be tailored to applications in various fields that are sometimes difficult to achieve with traditional components [19, 42].

Since the deformation logic is embedded in the architecture itself, metamaterial structures do not require additional components as the force-displacement behavior under stimuli is defined by the geometry. This approach allows the reproduction of components that have even better performance than their traditional counterparts. For instance, a study showed that traditional springs embedded in the foam of a vehicle seat can be replaced by metamaterial springs enabling better vibration isolation performance using nonlinear deformation. They also demonstrated that with geometric modifications they could obtain mechanical responses tailored to any application requirements [43] (see Figure 2.6A).

Metamaterials have also been used to create energy absorption structures by exploiting mul-

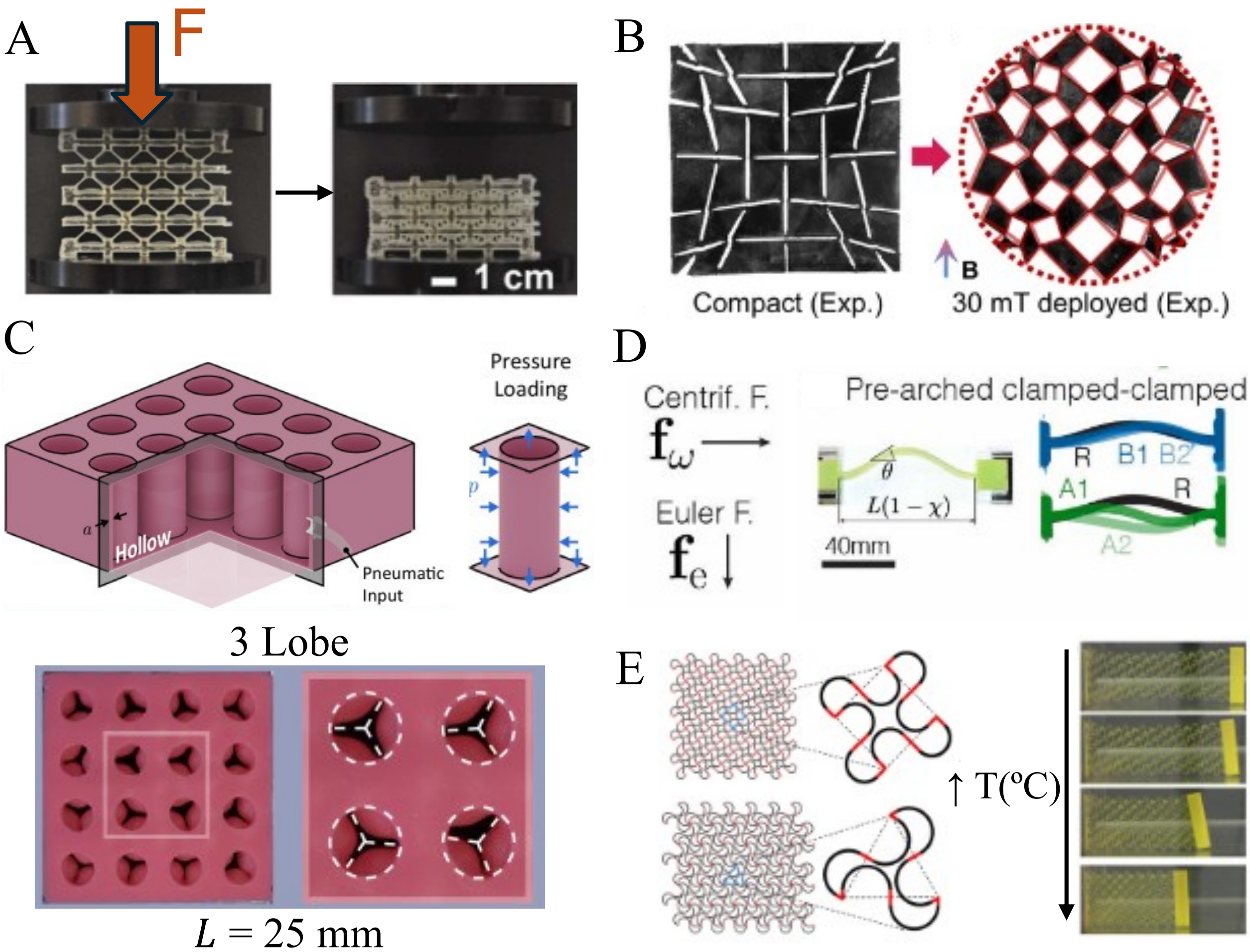

Figure 2.5 | **Actuation of lattice-based mechanical metamaterials. (A)** Compression of a von Mises truss-based structure under an external force [4] **(B)** Deployment of a lattice structure triggered by an external magnetic field [36] **(C)** Structural buckling of a thin-walled tube subjected to external pressure loading [37] **(D)** Deformation and snapping of a von Mises truss induced by centrifugal force [7] **(E)** Controlled deformation of a structure responsive to heating [40]

tistability and shape-reconfigurability for reusability. These shock-resistant structures can be used to keep intact an egg dropped from 1 m, while if the structure is pre-compressed, the egg breaks. Once the structure has been used to absorb an impact, it can be reset by pushing it for repeated use [44] (see Figure 2.6B).

Finally, in acoustic, metamaterials can be programmed to control sound waves for better sound transmission performance compared to traditional acoustic materials. By designing a unit cell with a tunable negative stiffness, a study showed that using it in an airplane cabin could reduce the noise inside the passenger's cabin while adding minimal weight compared to traditional heavier sound insulation materials [45, 46] (see Figure 2.6C).

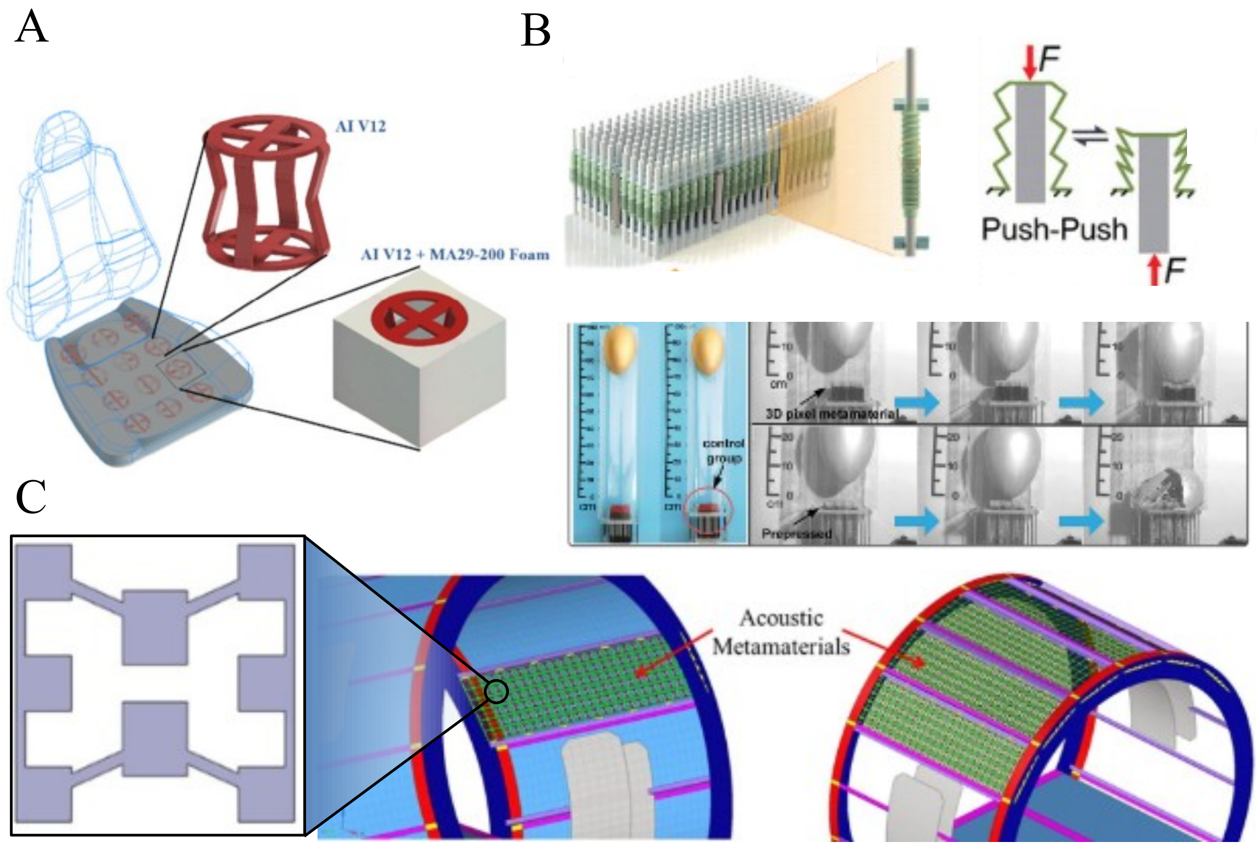

Figure 2.6 | **Engineering applications of mechanical metamaterials.** **(A)** Metamaterial structure that acts as a spring to achieve vibration isolation in vehicle seat [43] **(B)** Lattice metamaterial structure designs for energy absorption to be shock-resistant [44] **(C)** Metamaterial unit cell that can be used to reduce the noise inside the passenger's cabin in an aircraft [45]

2.7 Potential applications of mechanical metamaterials in the design of electric motors

While metamaterials can be used across different fields, they could offer promising utility through their integration into electric motors to increase their performance.

PMSMs are among the most efficient electrical motors used in the propulsion and transportation industry such as in the automotive industry due to their high power and torque density, efficiency, and compact size compared to traditional machines such as induction motors [47]. Figure 2.7A shows a representation of a PMSM. The key components include the permanent magnets (PMs), the rotor, and the stator. The stator is stationary, and the rotor with the PMs embedded rotates during operation of the motor [48].

In this thesis, we focus on Interior Permanent Magnet Synchronous Motors (IPMSMs). An

IPM motor is a type of PMSM in which the PMs are embedded inside the rotor core, rather than mounted on the rotor surface. The stator surrounds the rotor and has a predetermined number of poles, depending on motor and inverter design. The inverter is responsible for converting the direct current (DC) voltage from the battery into an alternating current (AC) voltage for the motor. In this case, the motor featured is based on the Toyota Prius design, which has eight poles with distributed winding. Figure 2.7B is a schematic that illustrates the geometry of a Toyota Prius motor and highlights these key elements.

However, PMSMs have a drawback: they are unable to efficiently maintain maximum torque at high speeds. Beyond a certain rotation per minute (rpm), flux-weakening techniques must be employed to prevent a rapid decrease in torque [49, 50]. In this thesis, we focus more particularly on mechanical flux-weakening strategies, and more precisely, self-actuated ones. Figure 2.7C shows how torque T, stator voltage u_s, flux linkage λ_{pm} and the current i vary with and without mechanical flux weakening. The torque T is defined as a function of u_s, λ_{pm} and i. The flux linkage λ_{pm} represents the magnetic coupling between the rotor PMs and the stator windings. As motor speed increases, the voltage required by the motor increases until it reaches the maximum level that the inverter can supply. If no flux weakening is applied, the torque drops sharply beyond this point, limiting the maximum speed to ω_{max1}.

With mechanical flux weakening, the voltage and current supplied to the motor are kept constant at their maximum levels, and the parameter that is reduced is the flux linkage. This allows the motor to reach a higher maximum speed ω_{max2}. Several passive mechanical methods for flux weakening have been proposed in the literature. Short-circuiting the flux is a method where a part made of a conductive material (such as a yoke) makes contact at some point with a part of the structure, diverting part of the flux away from the air gap and reducing flux linkage [51] (see Figure 2.7D). Another solution is to move the magnets away from the air gap, increasing the flux path length and decreasing flux linkage [52] (see Figure 2.7E). Also, flux weakening can also be done by blocking the flux path using iron pieces acting as flux barriers [53, 54] (see Figure 2.7F). All of these mechanisms rely on springs for linear displacements under centrifugal load of components such as yokes, magnets, or iron barriers. While these methods effectively achieve mechanical flux weakening, they increase system complexity and manufacturing cost by requiring additional components (e.g., springs) whose motion is programmed through rotational speed and centrifugal loading. More details on flux-weakening and the governing PMSM equations are provided in Appendix C.

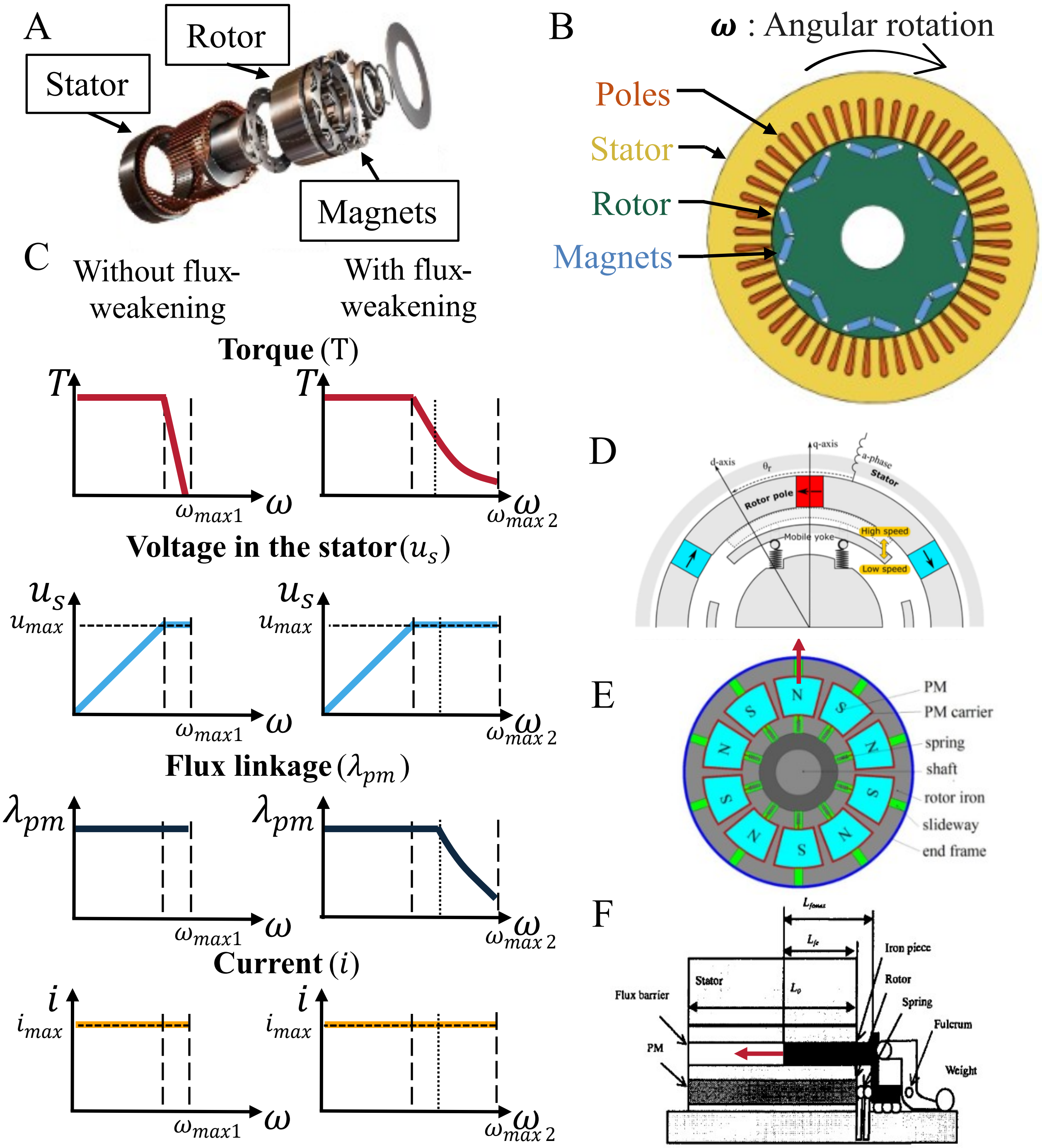

Figure 2.7 | **Electric motors. (A)** Representation of a PMSM [48] **(B)** Schematic of a PMSM motor highlighting key elements (based on a Toyota Prius motor) **(C)** Comparison of the torque, stator voltage, flux linkage and current with and without flux weakening **(D)** Short-circuiting the flux using a mobile yoke on springs [11] **(E)** Changing the position of the magnets away from the air gap using springs [52] **(F)** Blocking the flux with iron pieces [53]

CHAPTER 3 LITERATURE REVIEW SYNTHESIS AND THESIS OBJECTIVES

Metamaterials are engineered to provide unique mechanical properties through carefully designed geometry. Despite extensive research on metamaterials and their unconventional mechanical properties, few attempts have been made to harness centrifugal force as an actuation mechanism for structures such as the von Mises truss. Existing studies have primarily focused on stimuli such as displacement, pressure, or temperature, leaving rotational and inertial forces largely unexplored. This gap is particularly interesting to address because centrifugal force is inherently present in high-speed rotating systems and could enable passive, self-actuating mechanisms without the need for external control or complex algorithms. Moreover, very few studies propose potential applications for centrifugal force-driven unit cells.

The ability to control the displacement-rotation curve of a structure through its geometry and elasticity would open new possibilities for programmable mechanical responses tailored to specific applications. Developing tools to design and tune these curves could lead to adaptive systems that respond naturally to operating conditions, thereby reducing reliance on active control strategies.

Such an approach could enable the development of passive displacement mechanisms applicable across multiple domains, which represents the core objective of this thesis. A promising application is in PMSMs, where mechanical flux weakening could be achieved by embedding a metamaterial structure into the rotor geometry, thereby creating a displacement mechanism whose response is programmed through rotation and centrifugal loading. This solution could offer a promising alternative to traditional mechanical flux-weakening methods, with the potential to improve high-speed performance without increasing system complexity or cost. Accordingly, this thesis aims to develop a centrifugal force-driven meta-disk, and to do so, we propose three objectives:

- **Objective 1**: Design and simulate a meta-disk made of centrifugal force-driven unit cells
- **Objective 2**: Experimentally validate the simulation results of the meta-disk under tensile and centrifugal loading
- **Objective 3**: Programming the deformation of the meta-disk

To achieve these objectives, we propose the following methodology:

- **Objective 1 Methods**:
  - **1.1** Design a parametrizable meta-disk capable of exhibiting non-linear deformation
  - **1.2** Characterize the behavior of the unit cells in tension and under centrifugal loading via FE analysis
- **Objective 2 Methods**:
  - **2.1** Test the unit cells in the meta-disk in uniaxial tension to validate their tensile behavior
  - **2.2** Test the unit cells in the meta-disk under centrifugal loading to validate their rotational response
- **Objective 3 Methods**:
  - **3.1** Perform inverse design of the unit cells deformation in the meta-disk to match a target deformation under centrifugal force
  - **3.2** Apply the method to improve PMSM high-speed performance through mechanical flux weakening

CHAPTER 4 DESIGN AND SIMULATE A META-DISK MADE OF CENTRIFUGAL FORCE-DRIVEN UNIT CELLS

4.1 Geometry of the meta-disk

Figure 4.1A shows the meta-disk, composed of cyclic repeated unit cells. Each unit cell uses the von Mises truss, a simple and well-documented geometry, to achieve a nonlinear deformation response. By combining this structure with a block acting as a mass, a centrifugal force-driven unit cell is created. The geometry is parametrized by the variables: a, l, t_s, t_w, h_b, r, t_{gap} and d. The upper block has a height h_b and a width l. The von Mises truss at the bottom also has a width l, a slope a, and a thickness of t_s. The truss is connected to the block through a beam of width t_w. A t_{gap} separates the two elements. The bottom of the truss of the unit cell is placed at a distance r from the center of the meta-disk. The whole structure has a depth of d.

To facilitate the construction of a design space, three geometric ratios are also defined: $\frac{a}{l}$, $\frac{t_s}{l}$ and $\frac{t_w}{l}$. The parameters are based on the methodology of Rafsanjani et al. [20], and their definitions are illustrated in Figure 4.1A.

When the structure rotates at an angular speed ω, a centrifugal force F_c is generated. Under this loading, the structure deforms nonlinearly. We characterized the deformation by monitoring the displacement δ of the block. By tuning the parameters of the von Mises truss, the deformation under loading can be controlled, enabling control of the displacement-rotation response, or $\delta - \omega$ curve (see Figure 4.1B).

4.2 FE simulations of the unit cell

Now that the geometry is defined, we can proceed to the characterization of the deformation of the structure by monitoring the displacement of the block using the FE simulations in ABAQUS (version 2024) employing plane-stress elements (type CPS6). The material used is a Neo-Hookean hyperelastic incompressible material, with a Young's modulus of 2.88 MPa. The parameters are defined using the experimental stress-strain curve of samples molded in silicone Smooth-Sil 960. More details on the experimental values are provided in Section 5.2.

Figure 4.2A shows the configuration and boundary conditions of the static analysis simulation representing a tensile test performed on the structure. A vertical displacement δ is imposed at the top of the structure, and the reaction force F at the top of the beam is recorded. The

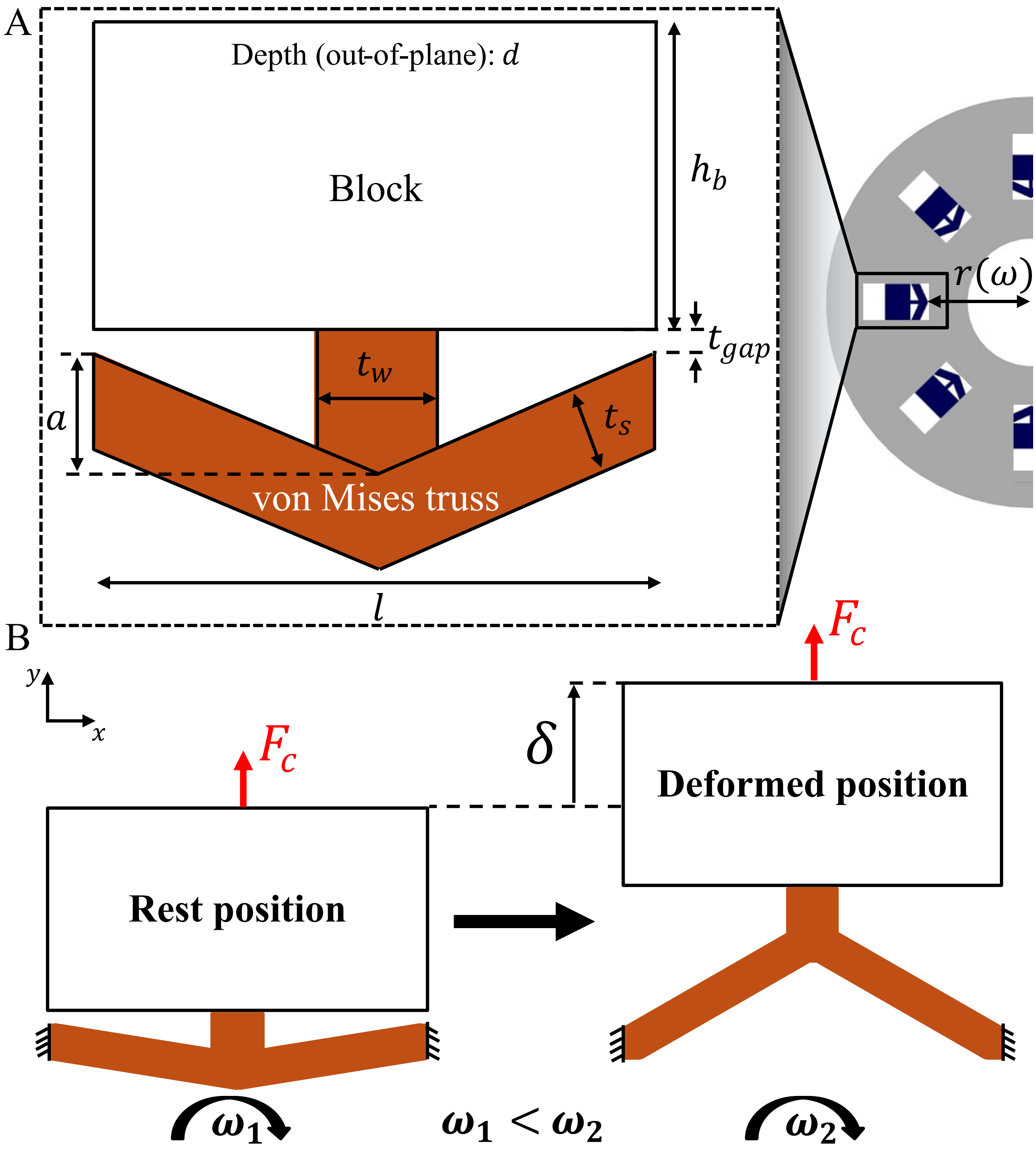

Figure 4.1 | **Metamaterial structure acting as a centrifugal force-driven meta-disk.** **(A)** The von Mises truss (orange) at the bottom of the unit cell is characterized by a width l, a slope a and a thickness t_s. The truss is connected to the upper block by a connector of width t_w, and a *gap* separates the two elements. The whole structure has a depth of d. The bottom of the von Mises truss is at a distance r from the center of the meta-disk. **(B)** At rest (low ω), the von Mises truss is not deformed. As the angular speed ω increases, the centrifugal force applied on the structure increases, which induces a nonlinear deformation of the truss and thus a displacement (δ) of the block.

sides of the structure are clamped by boundary conditions to prevent rigid-body motion.

We first consider four geometries. Their corresponding parameters $\frac{a}{l}$ and $\frac{t}{l}$ are listed in Table 4.1.

Table 4.1 | **Design parameters.** Values of $\frac{a}{l}$ and $\frac{t}{l}$ for the four geometries

Design	$\frac{a}{l}$	$\frac{t}{l}$
Design I	0.05	0.1
Design II	0.15	0.1
Design III	0.20	0.1
Design IV	0.45	0.1

Figures 4.2D-G show a representative force-displacement curve ($F - \delta$ curve) for each design under a static loading. To normalize the results, we define the non-dimensional displacement $\delta^* = \frac{\delta}{a}$, and the non-dimensional reaction force $RF = \frac{RF}{E \cdot d \cdot l}$, where E is the Young's modulus. We can see for Design I (see Figure 4.2D) that F increases monotonically with δ. For Design II (see Figure 4.2E), we can observe that an inflection point occurs at $\delta^* = 0.82$ where $\frac{d^2F}{d\delta^2} = 0$ and changes sign. For Design III (see Figure 4.2F), we can see that at $\delta^* = 0.54$, F stops increasing and starts decreasing. Then, at $\delta^* = 1.08$, F stops decreasing and starts increasing again, reaching the same reaction force before the decrease at $\delta^* = 1.39$. Finally, for Design IV (see Figure 4.2G), we can observe that at $\delta^* = 0.26$, F stops increasing and starts decreasing, reaching a negative force value. Then, at $\delta^* = 1.04$, F stops decreasing and starts increasing again, reaching the same reaction force before the decrease at $\delta^* = 1.60$.

We then study how the static response changes with the geometric parameters of the von Mises truss. Figure 4.2C presents a response map where the ratios $\frac{a}{l}$ and $\frac{t}{l}$ are varied. For simplicity, we define $\frac{t}{l} = \frac{t_s}{l} = \frac{t_w}{l}$. A mesh convergence was performed and is presented in Appendix A. In all the responses observed, we can characterize four families of curves based on the type of response: monotonic (green), transient (blue), snap (orange) and bistable (yellow). We observe that monotonic responses are only obtained at $\frac{a}{l} < 0.03$. For a $\frac{t}{l} = 0.1$, we have monotonic response at $\frac{a}{l} < 0.03$, transient response at $0.03 < \frac{a}{l} < 0.17$, snap response at $0.17 < \frac{a}{l} < 0.35$ and bistable response at $0.35 < \frac{a}{l}$. We can also observe that the domain range of bistable reduces when $\frac{t}{l}$ increases, stopping to exist when $\frac{t}{l} = 0.14$, while the transient and snap domains increase. Those results are in good agreement with the one obtained by Rafsanjani et al. [20].

Secondly, we want to study the structure behavior under rotation, as we aim to develop centrifugal force-driven unit cell. Figure 4.2B shows the configuration and boundary conditions of the dynamic analysis simulation representing a structure submitted to a rotation.

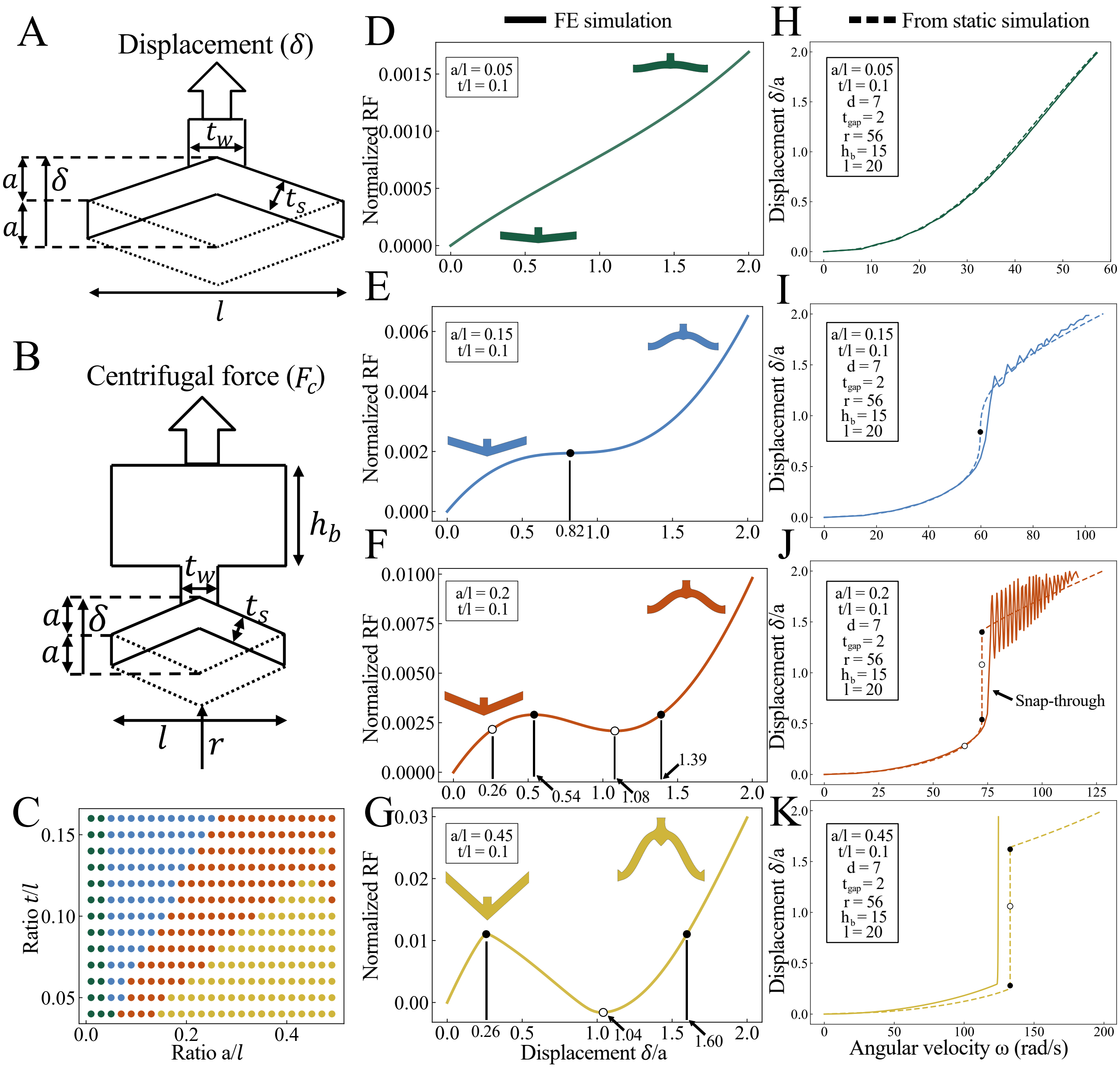

Figure 4.2 | **Results of the FE simulations.** **(A)** Definition of the static analysis simulation. A displacement δ is imposed at the top of the truss and the reaction force F is measured. **(B)** Definition of the dynamic analysis simulation. A rotation ω is imposed on the unit cell and the radial displacement δ is measured. **(C)** The static response under loading of the structure can be categorized in four types based on the ratios $\frac{a}{l}$ and $\frac{t}{l}$. Green: Monotonic, Blue: Transient, Orange: Snap, Yellow: Bistable. **(D)** Static results, Monotonic **(E)** Static results, Transient **(F)** Static results, Snap **(G)** Static results, Bistable **(H)** Dynamic results, Monotonic **(I)** Dynamic results, Transient **(J)** Dynamic results, Snap **(K)** Dynamic results, Bistable. All the results are obtained from FE simulations (Abaqus) using plane-stress CPS6 elements. All dimensions are in mm. $\rho = 1.25e^{-9}\frac{Ns^2}{mm^4}$.

As represented, an angular speed ω is imposed on the structure, and the radial displacement δ at the top of the block is measured. The structure is clamped on each side by boundary conditions. This rotation is applied as a body load equivalent to a centrifugal force over the entire structure. For a structure with a mass m located at radius r from the rotation center of the meta-disk and spinning at ω, the centrifugal force is defined as $F_c = m \cdot r \cdot \omega^2$.

Figures 4.2H-K present the deformation under rotation ($\delta - \omega$ curve) for each type of response under a dynamic loading. We can see for Design I (see Figure 4.2H) that δ^* increases rapidly as ω increases. For Design II (see Figure 4.2I), we can observe that near the inflection point $\delta^* = 0.82$ observed in the static analysis (see Figure 4.2E), there is a rapid increase of δ^* due to the reduction of $\frac{dF}{d\delta}$. For Design III (see Figure 4.2J), we can observe that the rapid increase of δ^* starts at $\delta^* = 0.54$ when F stops decreasing and ends at $\delta^* = 1.39$ when F reaches same reaction force than before the decrease (see Figure 4.2F). This behavior means that the structure exhibits negative stiffness, thus producing a snap-through segment in the "gap" region of the curve. Finally, for Design IV (see Figure 4.2K), we can observe the same behavior as Design III, snapping at $\delta^* = 0.26$ when F stops decreasing and ending at $\delta^* = 1.60$ when F reaches the same reaction force as before the decrease (see Figure 4.2G).

4.3 Static analysis curves to predict the dynamic analysis curves

Running dynamic simulations is computationally expensive and requires significantly more time than static analyses for the same geometry. For example, all static simulations require less than one minute to compute, whereas dynamic simulations take a minimum of two minutes for small $\frac{a}{l}$ configurations and can easily reach five minutes for larger $\frac{a}{l}$. The simulations were executed using 4 CPU cores in no-GUI mode via a Python script on a system with an AMD Ryzen 9 5900HS and 24 GB of RAM. Moreover, each geometric parameter influences the $\delta - \omega$ curve, and as a result, each parameter modification in a dynamic study requires a new simulation. For this reason, we explored a method to use the $F - \delta$ curve of a given geometry to predict the $\delta - \omega$ curve obtained from our dynamic analysis.

To accurately predict the $\delta - \omega$ curve, we first determine the relation between the rotational speed ω and the centrifugal force F_c. Using the definition of centrifugal force F_c, we can compute the value of the force applied on the structure for any rotational speed. By inverting this relation, the rotational speed is defined as a function of the force F, the mass of the structure m and the radius r. The new equation is $\omega = \sqrt{\frac{F}{m \cdot r}}$. We then use this relation in an iterative process. Initially, the structure is at rest meaning that $\delta = 0$. We define the radius as $r = r_{initial} + \delta$. $r_{initial}$ is defined as the radius between the center of rotation of the meta-disk and the center of mass in the structure. At each iteration, δ is increased by small increments. For each value of δ, the $F-\delta$ curve obtained from our static analysis provides the value of the force F required to deform the structure for this displacement. Using this force and the updated radius, we compute the rotational speed ω. The iteration then proceeds to the next displacement step. Figure 4.3 shows a simplified view of how the logic of the iterative process. Figure 4.2 shows a comparison between the four dynamic analysis curves previously presented in Figures 4.2H-K and the curves obtained using this prediction method (dashed line in Figure 4.2). In all four cases, both $\delta-\omega$ curves match, confirming the validity of the proposed technique.

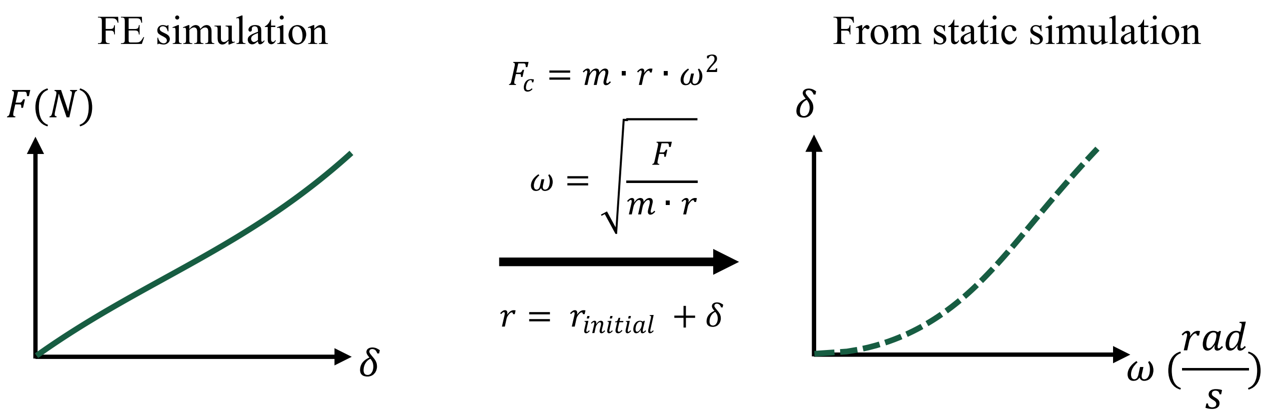

Figure 4.3 | **Static analysis curves to predict the dynamic analysis curves.** Schematic representation of the iterative procedure used to predict the dynamic $\delta - \omega$ response from the static $F - \delta$ curve

There is an edge case to take into account while running this script. It is when the computed value of ω for the new increment is lower than the previous value. This edge case happens when $\frac{dF}{d\delta} < 0$ like with Design III (see 4.2J) and Design IV (see 4.2K). It means that the structure has entered a snap-through region. In that case, we assign ω the previous higher value obtained, which leads to a displacement at constant ω.

This proposed technique is particularly useful, as it allows quick evaluation of the behavior of a structure under rotation with any parameters. It reduces analysis time and serves as an efficient tool to quickly compare the performance of any centrifugal-force driven unit cell.

4.4 Unloading behavior

We now examine whether the structure exhibits hysteresis between the loading and unloading of the force as in practical application the rotational speed increases and subsequently decreases back to rest. We use our script describe in Section 4.3 to simulate the behavior of each sample in a dynamic analysis in which the angular speed ω is increased then decreased.

The results are presented in Figure 4.4 and show the behavior of each case under such cyclic loading.

Figure 4.4A (Monotonic) shows that the $\delta^* - \omega$ curve is perfectly coincident in both directions, indicating no hysteresis. Figure 4.4B (Transient) exhibits similar behavior with no hysteresis. In comparison, Figure 4.4C (Snap) displays clear hysteresis. During the increase of ω, the snap-through happens when the centrifugal force reaches the local maximum of the snap region identified in the static response in Figure 4.2F. When ω reduces, the snap-through only happens when the centrifugal force reaches the bottom of the "gap" of this snapping region. This behavior can be easily explained by examining the reference static loading curve $F - \delta^*$ and by re-plotting it in the $\delta^* - F$ referential. Finally, Figure 4.4D (Bistable) shows that, after snap-through, the structure remains in the new stable state and does not return to its initial state even when reducing ω, which is characteristic of bistability.

During the simulation of the bistable case, we ran into another edge case of the script when $F < 0$. It means that the structure is bistable like Design IV. In that case, during unloading, the script needs to take into account that there is a stable state $\delta^* = 1.04$, and that, without external loading, the structure can not deform beyond this δ^* value.

We can observe a discrepancy between the predicted and simulated results, which increases with larger values of $\frac{a}{l}$. This is expected as, with the script, the snap-through is defined exactly at the δ^* where the static $F - \delta^*$ curve starts decreasing. In contrast, the dynamic simulations where a load is imposed are subject to some instabilities that can impact the ω at which the snap-through happens.

Characterizing the loading-unloading response is important for selecting the appropriate type of response based on a given use case. For instance, when a consistent displacement path is required during both loading and unloading, it is necessary to use a monotonic or transient structure, and the transient structure can provide a snap-like displacement while having a displacement similar. Snap structures provide a snap and can be used in applications where it is useful to have the displacement at two different rotation speed. Finally, the bistable family can be used in applications where the structure should remain deployed in a second stable state once activated.

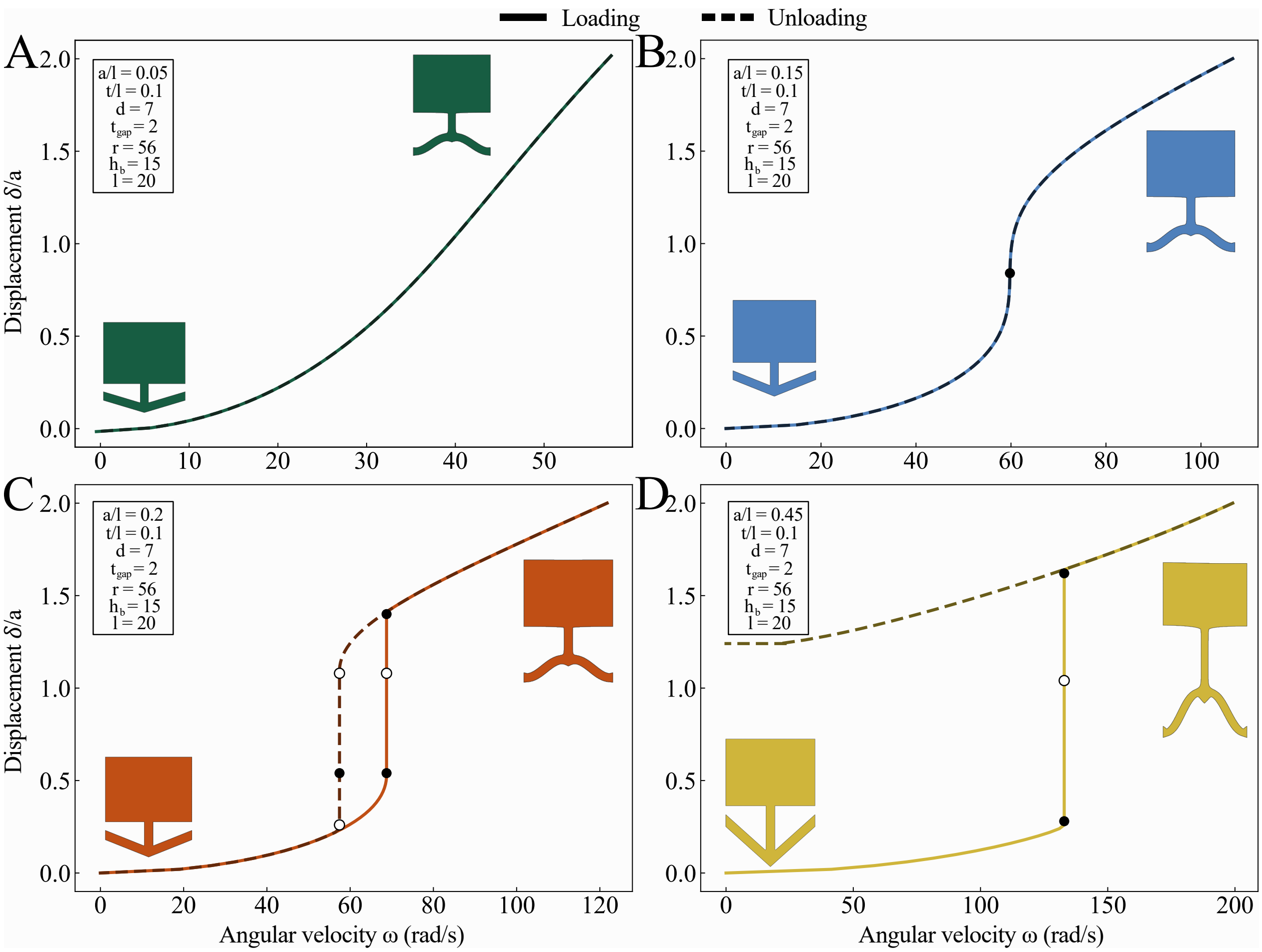

Figure 4.4 | **Results of the loading-unloading analysis.** Response type obtained under loading-unloading analysis for the four types of response obtained during the static analysis. Hysteresis appears only for snap-through responses. Under increasing rotation, snapping occurs at a higher ω than the snap-back observed during the decrease of ω. **(A)** Monotonic **(B)** Transient **(C)** Snap **(D)** Bistable. All the results are computed using the static analyses from FE simulations (Abaqus) using plane-stress CPS6 elements. In the bistable case, after snap-through, the structure remains in the new stable state and does not return to its initial position during the reduction of ω. All dimensions are in mm. $\rho = 1.25e^{-9}\frac{Ns^2}{mm^4}$.

CHAPTER 5 EXPERIMENTALLY VALIDATE THE SIMULATION RESULTS UNDER TENSILE AND CENTRIFUGAL LOADING

5.1 Fabrication

To experimentally validate the FE simulation results, we fabricate unit cell samples using silicone rubber. Three samples are produced for each type of response behavior: monotonic (Design I), transient (Design II), snap (Design III), and bistable (Design IV).

Figure 5.1A shows four fabricated unit cell samples, representing a sample for each type of response behavior. A standalone sample is composed of three parts. Figure 5.1B shows separately each of these parts. The deformable section is molded in a single piece using silicone rubber Smooth-Sil 960 and a 3D-printed negative mold made of Polylactic acid (PLA). To prevent unintended buckling of the lower truss during testing, external and internal PLA components are added acting as reinforcement pieces.

Figure 5.1C presents the dimensions of the printed parts for a ratio $\frac{a}{l} = 0.05$. The dimensions of each mold vary slightly depending on the desired geometric ratios. In our testing, the ratio $\frac{t}{l}$ was kept constant, while the ratio $\frac{a}{l}$ was varied. Each sample has a total length of 20 mm and a thickness of 2 mm. The upper block has a width of 10 mm and a length of 15 mm. These dimensions were selected to ensure proper clamping and prevent slippage during tensile testing.

The 3D printer used for fabrication is the Bambu Lab X1E from Bambu Lab, and the PLA filament is ELEGOO PLA White 1.75mm from ELEGOO. The silicone rubber used is Smooth-Sil 960 from Smooth-On, and the mold release agent applied to facilitate demolding is Easy Release 200, also from Smooth-On.

The molding process for the silicone component is described below, and all elements of the process are shown in Figure 5.2.

1. **Step 1 :** Apply a mold-release agent (Smooth-On Easy Release 200) to the mold to facilitate demolding.

2. **Step 2:** In a mixing cup, prepare the silicone (Smooth-Sil 960, Smooth-On) at the recommended ratio (100A:10B). Mix thoroughly and degas the mixture in a vacuum chamber to remove entrapped air.

3. **Step 3 :** Pour the silicone into the mold. Place a flat plate in acrylic (with mold-release

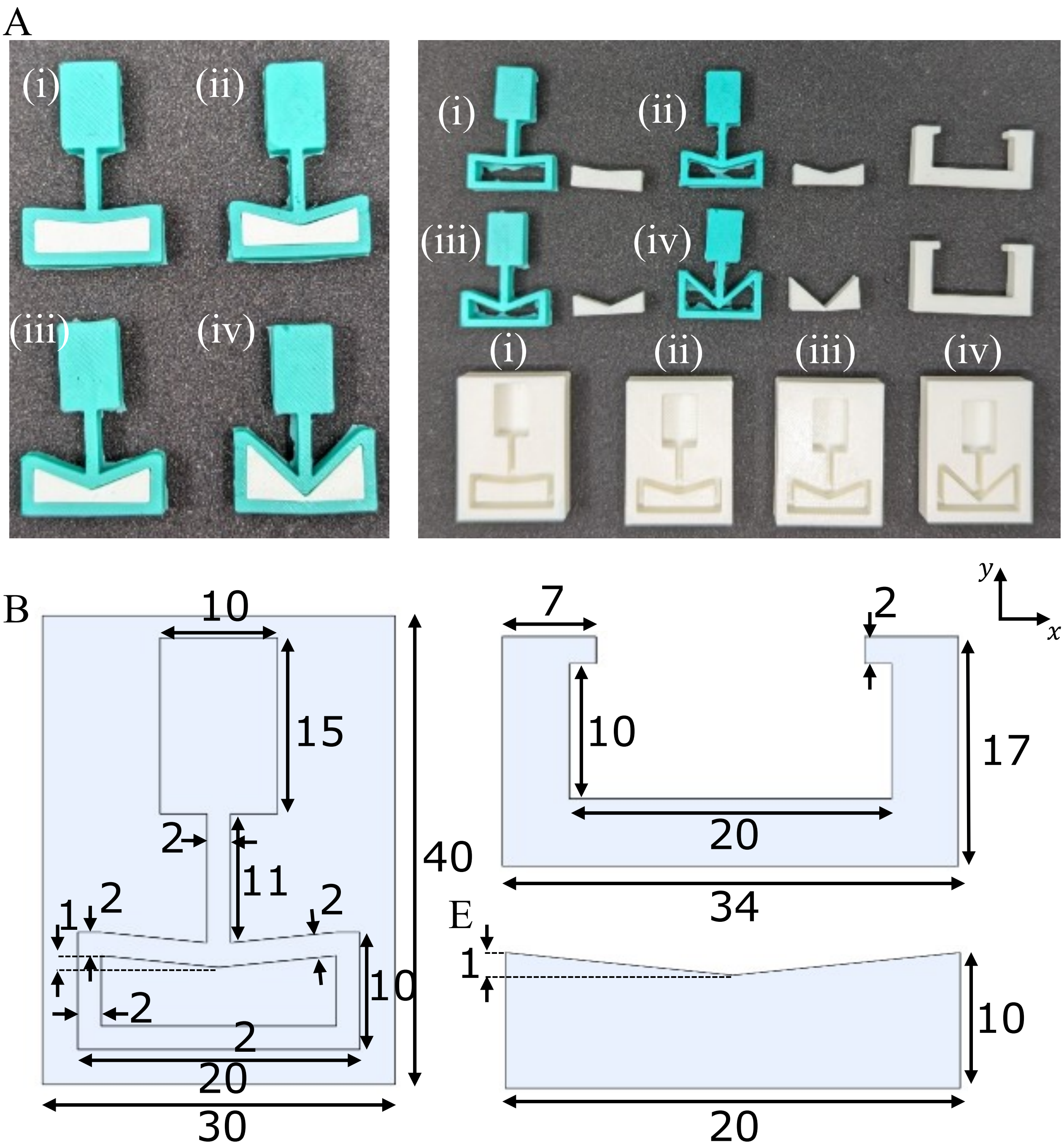

Figure 5.1 | **Sample of a unit cell fabricated.** **(A)** Fabrication of a unit cell sample for each type of response behavior. Each sample is made of 3 parts. [**i**]: Monotonic [**ii**]: Transient [**iii**]: Snap [**iv**]: Bistable **(B)** A negative mold is used to cast the deformable silicone component. Two PLA pieces are used to constrain the deformation of the unit cell. An external part is located around the base and the other is inside in order to prevent the buckling of the bottom section of the structure. All dimensions are in mm.

agent sprayed on it) on top with weights. Wait for the silicone to cure fully (around 24h) before demolding.

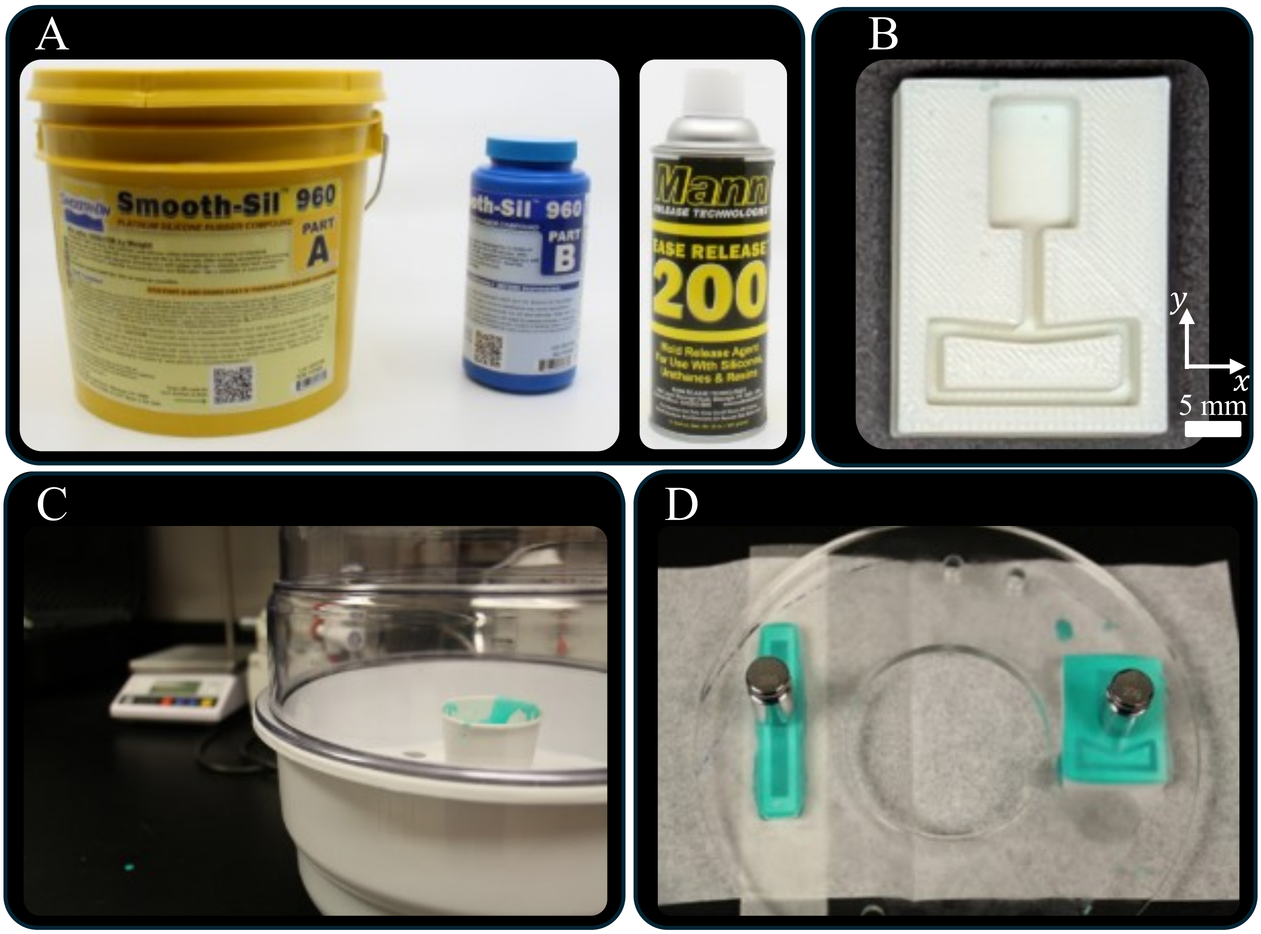

Figure 5.2 | **Molding process.** **(A)** The materials needed for the molding process are silicone rubber (Smooth-Sil 960, Smooth-On) and mold-release spray (Easy Release 200, Smooth-On) **(B)** The silicone is poured into a 3D-printed PLA negative mold replicating the unit cell geometry **(C)** A precision balance ensures the correct 100A:10B mixing ratio, and a vacuum chamber is used to degas the mixture **(D)** An acrylic plate with weights is placed on top of the mold during curing to ensure a flat, uniform surface

5.2 Static tensile testing

To validate the FE simulation results, uniaxial tensile tests are conducted on the silicone samples. The tests are performed using a Biomomentum Mach-1 v500c mechanical tester equipped with a 100N load cell. For each sample, a displacement of $\delta = 2a$ is imposed. A displacement rate of 0.1 mm/s is applied for all tests.

Figure 5.3A shows the experimental setup for the tensile testing used to test a rectangular specimen, with dimensions of 50 mm x 5 mm x 3 mm (LxWxt) of the silicone rubber to experimentally determine the Young's modulus. The resulting force-displacement curve, combined with the measured initial and final lengths, and cross-sectional area, is processed into a stress-strain curve needed to determine the elasticity property. Figure 5.3B shows the stress-strain curve obtained. Since the resulting curve is nonlinear, a purely elastic model is insufficient. Instead, a hyperelastic model is required. The Neo-Hookean model is selected as it is well-suited for silicone rubber materials. The Neo-Hookean model is defined as:

$$\sigma = 2C_{10}(\lambda - \frac{1}{\lambda^2}) \tag{5.1}$$

where $\lambda = 1 + \epsilon$, and ϵ is the engineering strain. The most fitting parameter for the Neo-Hookean that we obtained is C_{10}=.48. We can then calculate Young's modulus using $E = 2G(1+\nu)$. We assume a Poisson's ratio $\nu = 0.5$ as silicone is a nearly incompressible material. Therefore, we obtain a Young's modulus of $E \approx 6C_{10} = 2.88$ MPa. This value is coherent with those reported in the literature for Smooth-Sil 960 and with the specifications provided by the manufacturer [55–57]. These values are the ones used in the FE simulations presented in Figure 5.5.

Figure 5.4 shows the experimental setup for the tensile testing used to test four unit cell geometries with a length $l = 20$ mm representing each type of response (monotonic, transient, snap, bistable). All samples have $\frac{t}{l}$=0.1, and we varied $\frac{a}{l}$ to obtain a sample representing each category based on the response map obtained in Section 4.2 and presented in Figure 4.2C.

Figure 5.5 compares the experimental force-displacement curves obtained from tensile testing with the corresponding FE simulation results for the four response types. For the monotonic case (see Figure 5.5A), the two curves exhibit the same behavior under deformation but differ in magnitude. For the transient case (see Figure 5.5B), the FE simulation is able to capture the inflection behavior. For the snap case (see Figure 5.5C), the negative stiffness property is well captured by the FE simulation. Finally, for the bistable case, the negative force is capture by the FE simulation (see Figure 5.5D). Overall, there is a good agreement between the experimental and FE simulation curves in all cases, validating the accuracy of the simulations. Minor discrepancies may be attributed to the fabrication of the samples and slight misalignments during the mounting of the samples in the tensile testing machine

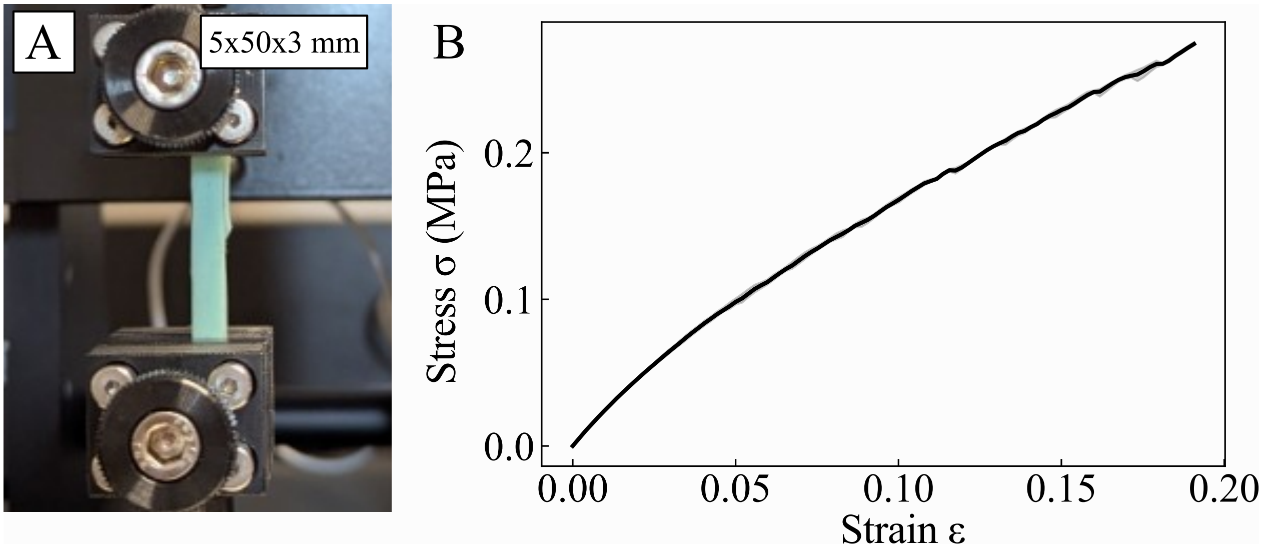

Figure 5.3 | **Stress-strain curves characterization of silicone Smooth-Sil 960 from Smooth-On. (A)** Experimental testing to obtain the force-displacement curves of unit cell samples using the Biomomentum Mach-1 v500c mechanical tester (100N load cell). Rectangular beam to measure the Young modulus. **(B)** Experimental stress-strain curve obtained from a rectangular specimen beam sample to determine the Young's modulus **Legend:** Mean values of three samples (solid line) and minimum and maximum ranges (shaded area) are shown

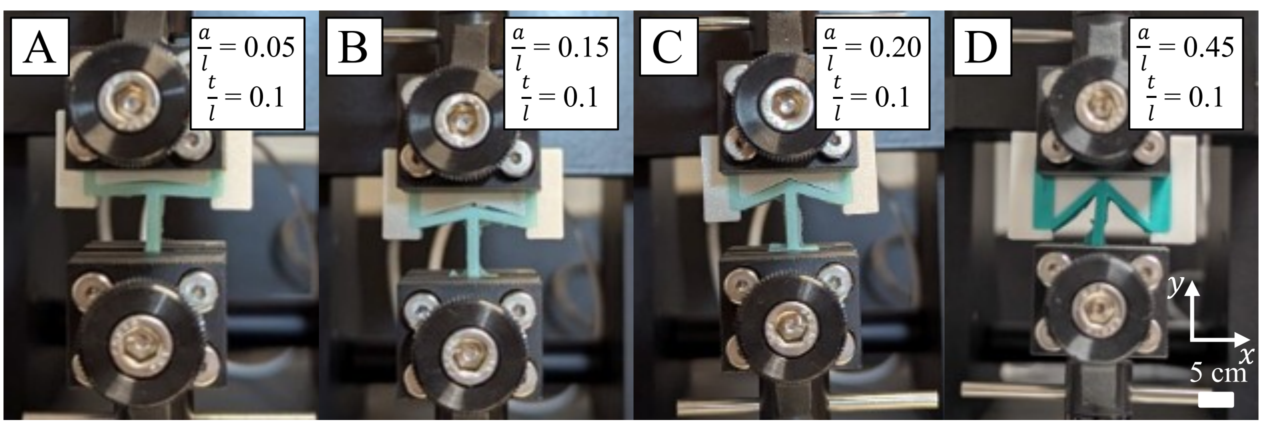

Figure 5.4 | **Tensile testing.** Experimental testing to obtain the force-displacement curves of unit cell samples using the Biomomentum Mach-1 v500c mechanical tester (100N load cell). All samples have $l = 20$ mm **(A)** Monotonic **(B)** Transient **(C)** Snap **(D)** Bistable

5.3 Dynamic rotation testing

Figure 5.6 shows the custom test bench conceived and built. To simplify displacement tracking, a camera is mounted directly on the rotating shaft. This configuration ensures that the

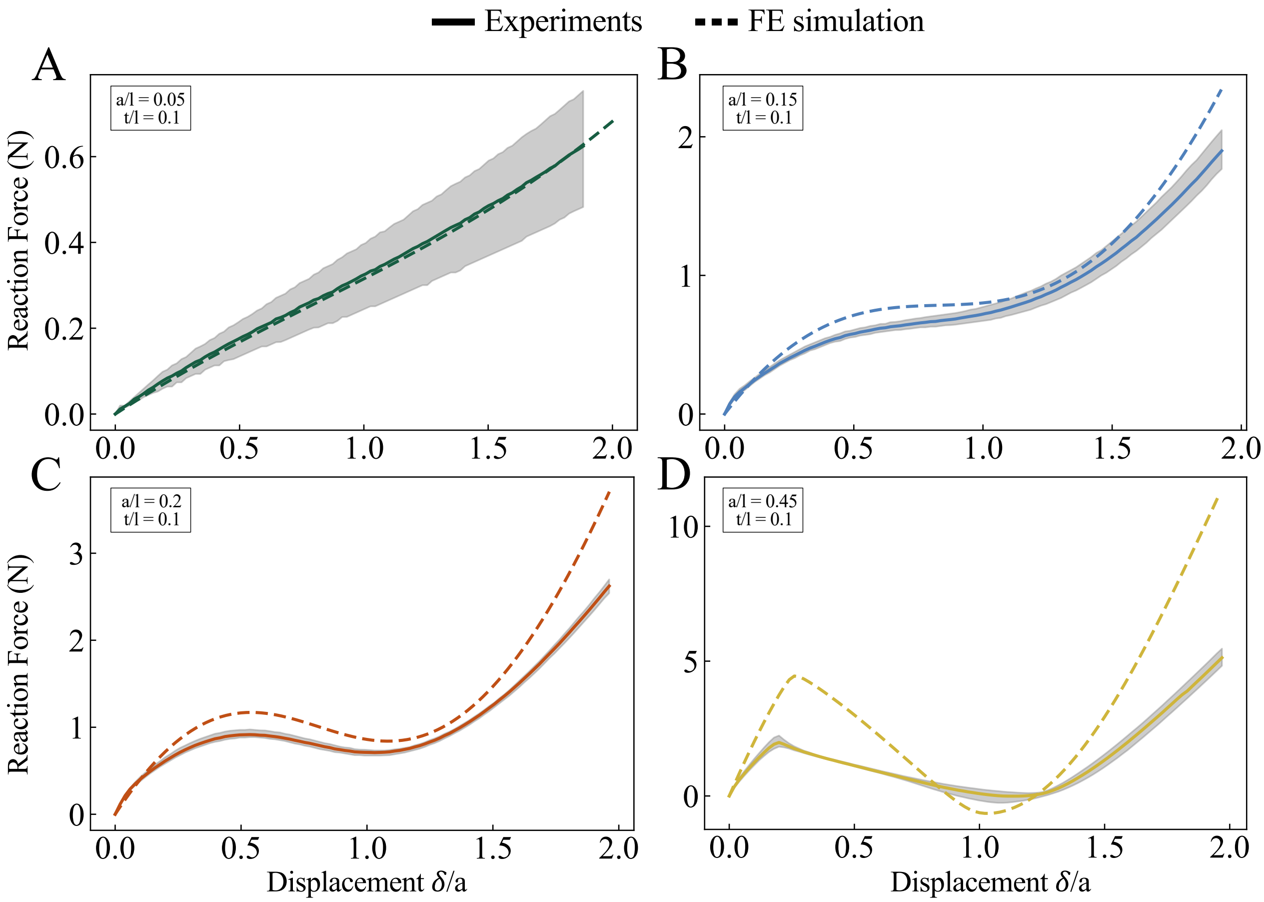

Figure 5.5 | **Comparison of the force-displacement curves obtained by experimentation and FE simulations.** Uniaxial tensile tests done on unit cell samples are compared with the corresponding FE simulation results for the four types of response **(A)** Monotonic **(B)** Transient **(C)** Snap **(D)** Bistable. The gray shaded region around the curve represents the deviation across three samples, while the curve shows the mean value.

sample remains stationary in the camera frame during the entire test. High-speed rotation is achieved using a 12-24V DC motor capable of reaching 10000 rpm under no-load. Counterweights are added on the camera arm to balance it, and a vibration damping shaft coupler is incorporated to minimize vibrations and thus enable higher stable rotational speeds. Lastly, a fixed Hall-effect sensor is mounted on a beam fixed on the optic table in a way that the strong magnet placed under the sample-holding arm is passing near. The output allows precise measurement of the actual rotation speed of the sample during testing.

To validate the precision of the tracking software Kinovea used to track the displacement from video recordings. We compare the precise and known displacement provided by the Biomomentum Mechanical Tester Model Mach-1 v500c with the displacement measured by Kinovea. Figure 5.7 shows the comparison for a known displacement rate of 1 mm/s. There is

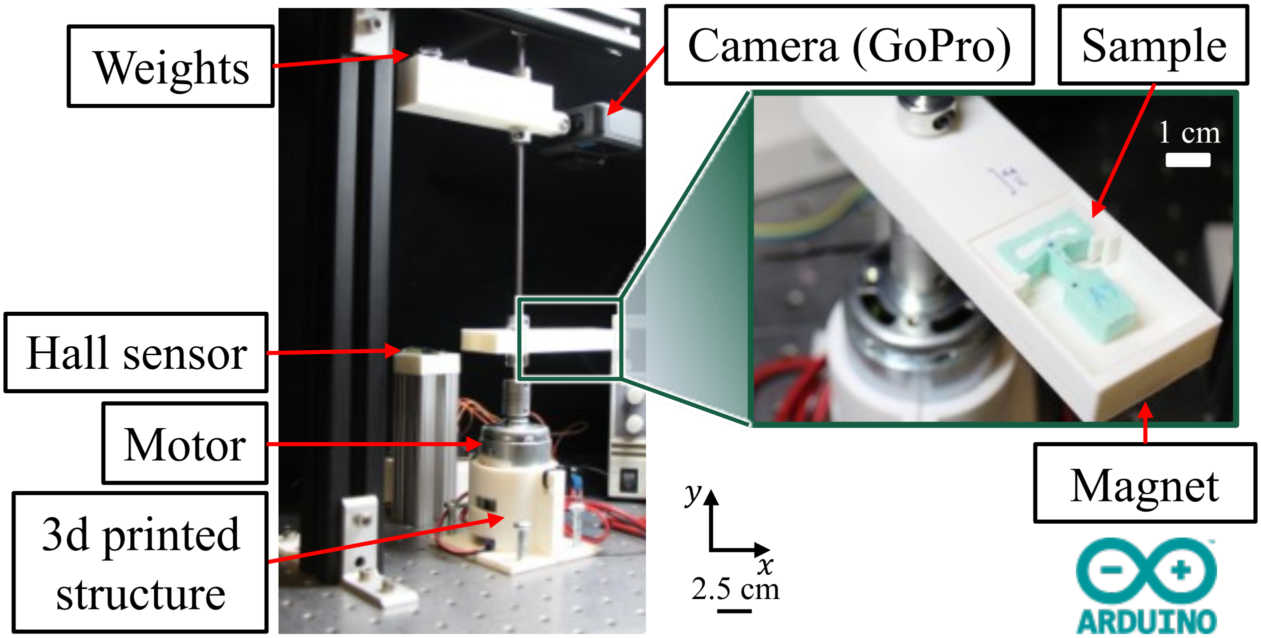

Figure 5.6 | **Presentation of the custom test bench conceived and built.** The test bench built is using a motor mounted on an optic table by a 3d printed structure. A GoPro camera records the deformation of the sample and a Hall-effect sensor paired with a magnet measure the rotational speed. All the data and the control is processed via an Arduino Uno.

a good agreement between the two measures, confirming the validity of the tracking method for dynamic testing.

We carry out dynamic tests at multiple rotation speeds. For each test, we apply a constant motor voltage, allowing the system to reach and maintain a steady rotation speed. The rotation speed is measured in real time using a Hall-effect sensor connected to an Arduino, which then transmits the data to a computer. The electric schematic is presented in Appendix B. The deformation of the sample is recorded using a GoPro camera operating at 8K resolution and 240 frames per second (fps), in linear mode. Using Kinovea, the radial displacement of the sample is extracted over a 1s interval at constant speed.

Figure 5.8 compares the displacement obtained experimentally at multiple rotation speeds with the displacement predicted using the FE static simulation results obtained using Abaqus. We can observe that for the monotonic case, the experimental data follow the general trend of the predicted curve, although small discrepancies are visible. Those differences can be explained as the deformation at this ratio is really small, reducing the accuracy of the displacement measurements. For the transient and snap case, the experimental results closely match the predicted curve. The rapid increase in displacement is even obtained on the transient sample. As for the snap, we can clearly observe the snap-through on the recordings.

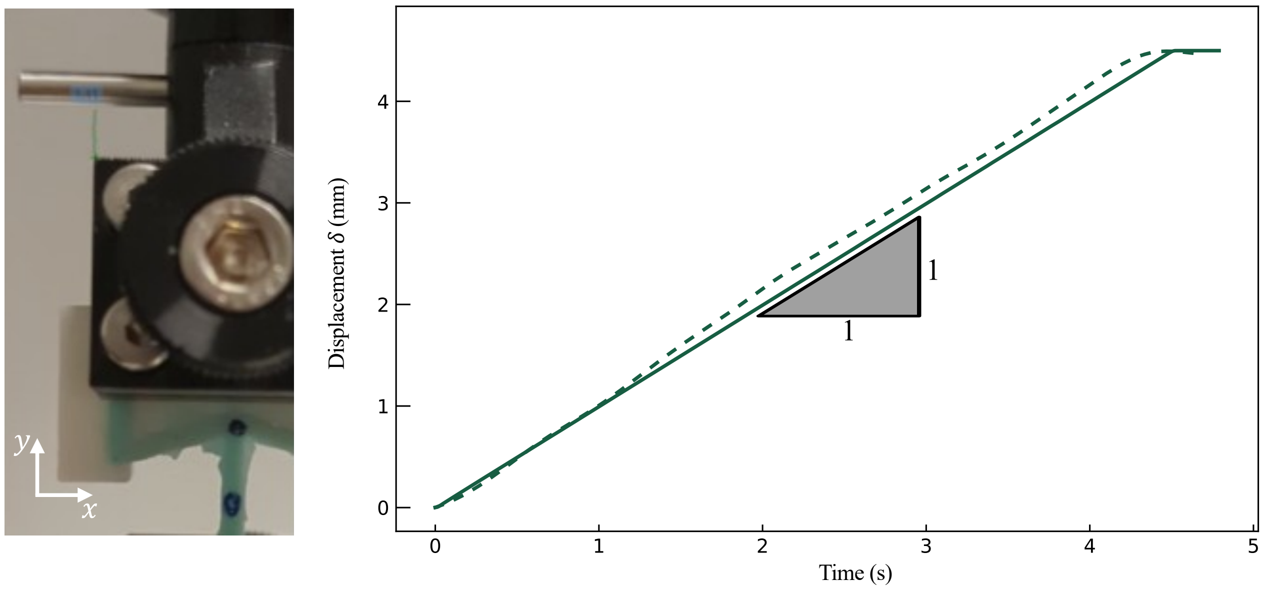

Figure 5.7 | **Validation of the tracking software.** Comparison between the displacement measured from recording using Kinovea with the reference displacement imposed by the Biomomentum Mechanical Tester Model Mach-1 v500c for a known displacement rate of 1 mm/s. **Legend:** Reference (solid line) and measured (dashed line) displacement are shown

The experimental results closely match the predicted curve before and after the snap. For the bistable, the experimental results closely match the predicted curve before the snap. However, the snap does not happen at the same rotational speed as predicted using the FE static simulation result. This discrepancy can be attributed to differences between the reaction forces measured experimentally and those obtained from the FE simulation (see Figure 5.5D). We can also observe the bistability experimentally, as the units remain in a new stable state after snapping and unloading. Note that an additional mass of 5 g was added to ensure that snapping occurs within the operating speed window of the test bench. Overall, we observe good agreement between the experimental data and the simulation results across all response types.

These results show that it is possible to fabricate centrifugal-force driven unit cells that behave closely to their simulated counterparts. This validation is essential, as it confirms that a given unit cell geometry will exhibit in reality the same static and rotational behavior as predicted by the simulations.

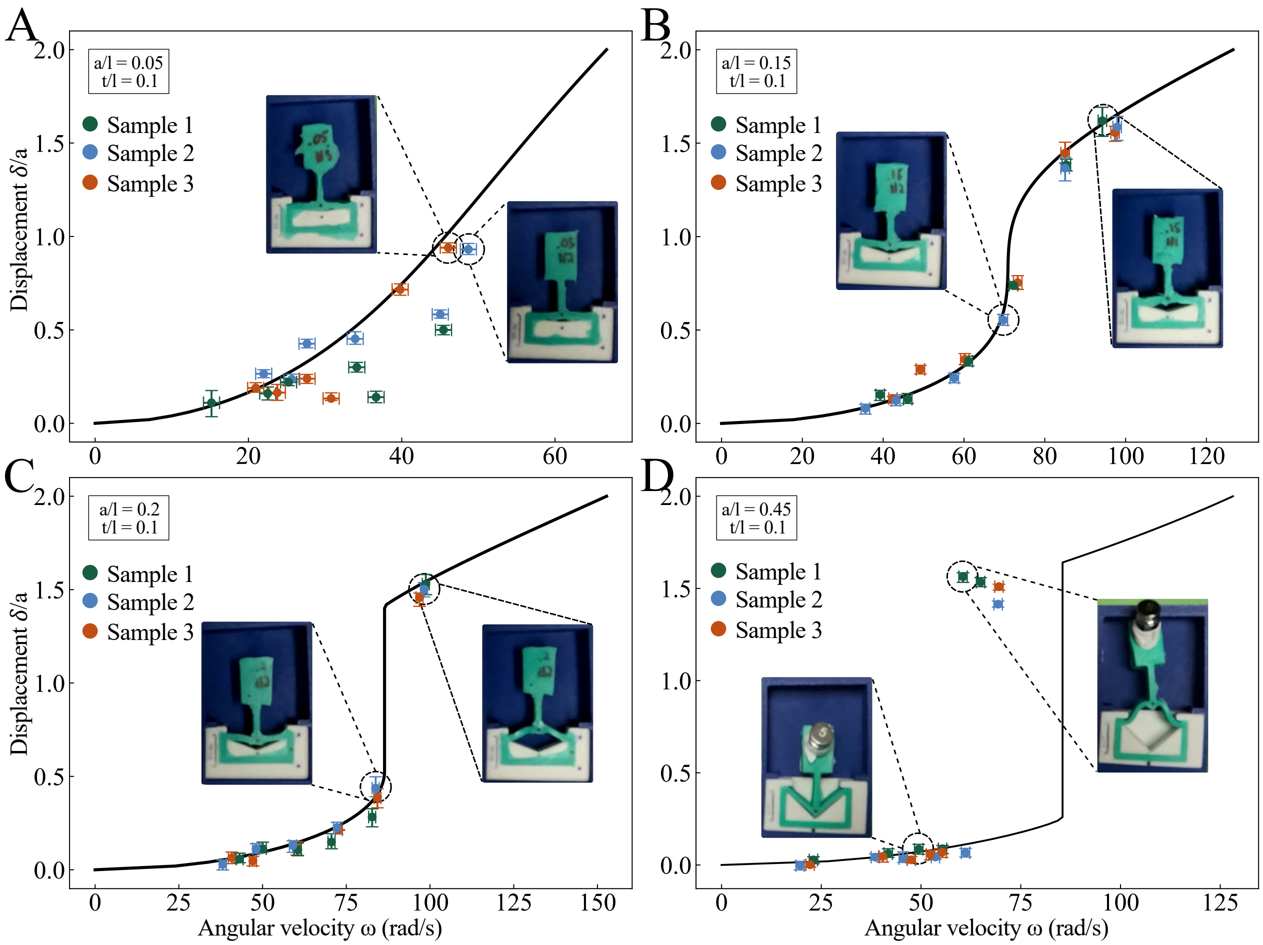

Figure 5.8 | **Comparison of the displacement under rotation of the sample obtained by experimentation and FE simulations.** Comparison between the displacement obtained experimentally at multiple rotation speeds with the curves obtained using the prediction method based on static simulations using Abaqus for unit cell of each response type. The displacement was filmed in 8k 240fps using a GoPro in linear mode. The tracking of the displacement for the experimentation was done using Kinovea. **(A)** Monotonic **(B)** Transient **(C)** Snap **(D)** Bistable. Error bars in x-direction represent the variation in displacement at steady speed over 1 s, and the error bars in y-direction represent the variation in rotational speed over the same interval.

CHAPTER 6 PROGRAM THE DEFORMATION OF THE META-DISK

6.1 Control of the deformation

With the deformation of the unit cell characterized as a function of the rotation, we next perform inverse design of the meta-disk to program its deformation under rotation. Figure 6.1A illustrates the inverse-design process.

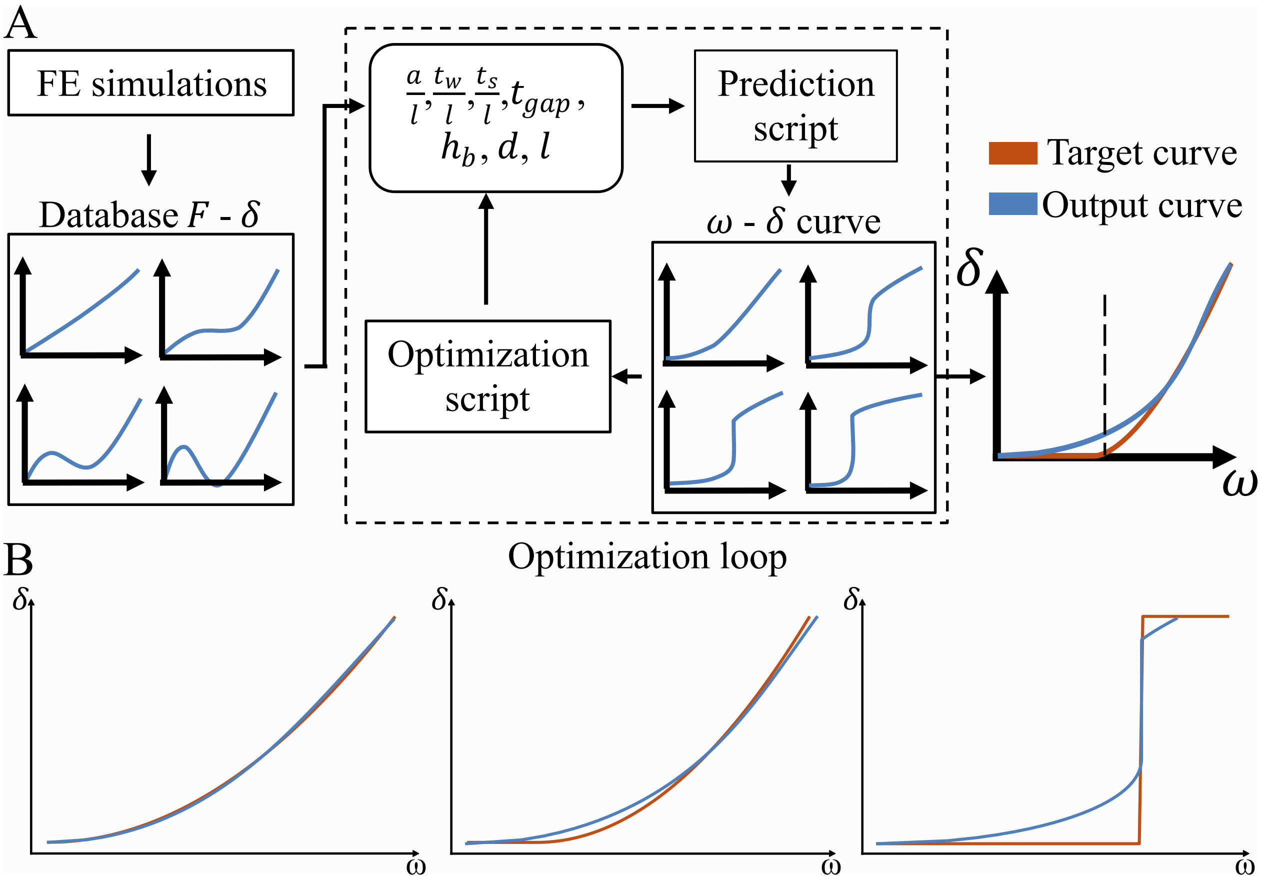

Figure 6.1 | **Control the δ-ω curve.** **(A)** Workflow for unit cell parameter optimization. Using the $F - \delta$ curves obtained with FE simulations, a Python prediction script to obtain the $\delta - \omega$ response, and a Python optimization script, the best unit cell parameters are identified. Those parameters give an output curve representing the $\delta - \omega$ response under rotation (blue) that closely matches the target curve (orange), allowing for the control of deformation under rotation for any application. **(B)** Example of target (orange) and output (blue) displacement-rotation curves are shown

Based on a specific application or use case, a target displacement-rotation (δ—ω) curve (shown in orange) is defined. This curve represents the deformation wanted of the unit cell at each rotation speed. The goal is then to identify the geometric parameters ($\frac{a}{l}, \frac{t_w}{l}, \frac{t_s}{l}, t_{gap}, h_b, d, l$) that give a unit cell whose displacement-rotation curve (shown in blue) best matches the wanted curve. In order to obtain these results, three components are required: (i) all the force-displacement curves obtained from static FE simulations, (ii) a Python script implementing the prediction algorithm to obtain the $\omega - \delta$ curve, and (iii) a Python optimization script designed to select the force-displacement curve that best matches the target curve. For the optimization script, the strategy involves evaluating all available curves and comparing them to the target curve. To quantify the similarity between curves, we chose to use the Mean Squared Error (MSE) metric due to its simplicity and ease of implementation. Lastly, several user-defined constraints must be specified: (i) r, the radial distance between the rotation center and the unit cell; (ii) l, the width of the unit cell; and (iii) the material properties, specifically the Young's modulus E and the density ρ. These have an important influence on the resulting δ-ω curve and this allows to get only feasible geometries after running the algorithm. Note that for simplification, we use the design space of all the force-displacement curves obtained from static FE simulations which uses $\frac{t}{l} = \frac{t_w}{l} = \frac{t_s}{l}$. As shown in Figure 6.1B, this method allows the output of a response curve that closely matches the target curve across various shapes. This demonstrates that the method can be used and adapted to different applications with different requirements.

6.2 Obtain the optimal displacement-rotation curve to maximize torque in a PMSM

We explore the potential of using a programmable meta-disk to improve the performance of PMSMs. As mentioned in Section 2.7, after reaching a certain rotational speed, the torque of PMSMs starts to reduce quickly. To maintain torque at higher speeds, a mechanical flux-weakening strategy can be employed. This solution, which is an alternative to current-based methods, aims to physically reduce the magnetic flux linkage between the magnets in the rotor and the poles in the stator. Flux weakening must start at the base speed ω_{base}, when the voltage required by the motor reaches the inverter limit due to the back-electromotive force (back-EMF). The inverter converts the DC voltage supplied by the battery into an AC voltage for the motor. Since the back-EMF is proportional to the rotational speed ω and the flux linkage λ_{pm}, increasing ω beyond this point requires a reduction of λ_{pm} in order to maintain maximum torque T at higher speeds.

Figure 6.2 illustrates the process from the conception of a mechanical flux-weakening solution to the obtention of the target displacement-rotation curve that the unit cell must achieve. Once the electric motor is chosen, the first step (Figure 6.2A) is to quantify the variation of the flux linkage as a function of the mechanical displacement δ of the adjusters in the flux-weakening mechanism, giving the λ_{pm}–δ relation. For each speed increment ω, the simulation then maximizes T based on the motor's current and voltage limits (Figure 6.2B). When the voltage limit is reached, the software identifies the required reduction of λ_{pm} that allows further increases in ω while still maximizing T. This iterative process gives the optimal flux linkage λ_{pm}-ω relation. The final step (Figure 6.2C) is to link the optimal flux-linkage values from step B back to their physical displacement in step A to obtain the optimal displacement of the mechanism as a function of ω that maximizes T. Knowing λ_{pm}-δ from step A and the optimal λ_{pm}-ω from step B, we obtain the target δ-ω curve that our unit cell needs to match.

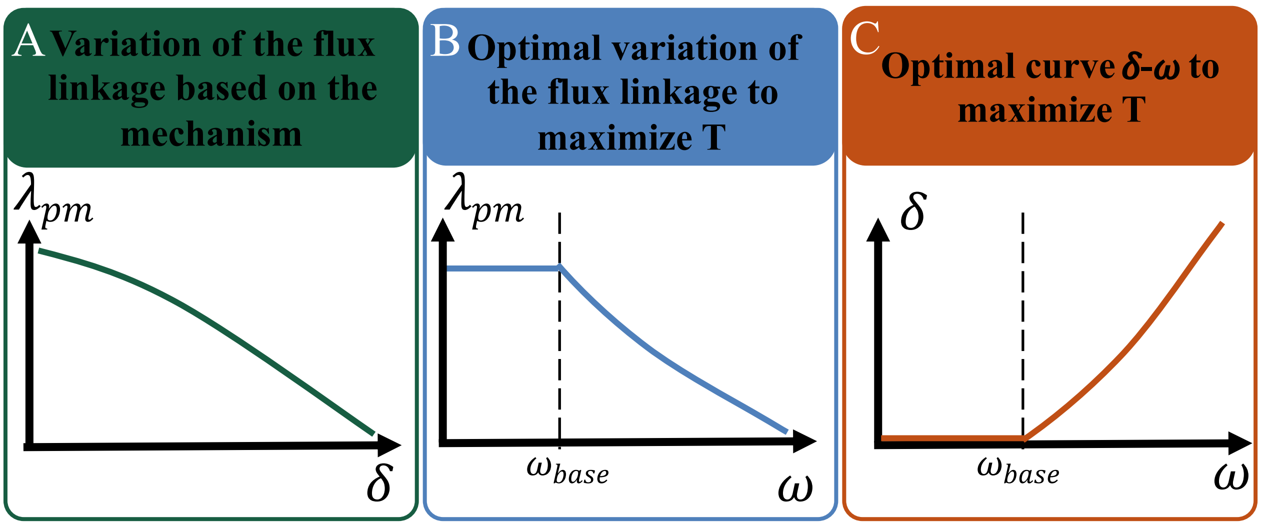

Figure 6.2 | **Determining the target δ-ω curve to maximize the torque.** **(A)** Flux linkage based on the mechanism displacement (λ_{pm}-δ) **(B)** Optimal variation of λ_{pm} based on the rotational speed ω to maximise the torque T (λ_{pm}-ω) **(C)** Combination of the curve A and the curve B to obtain the target mechanism displacement based on the rotational speed that maximizes torque (δ-ω) *Note: The curves presented here are examples to aid in understanding*

6.3 Defining the mechanical flux-weakening concept

We choose to implement a mechanism that reduces the permanent magnet flux passing from the rotor to the stator by locally short-circuiting the flux. Figure 6.3A shows in details the concept and its final dimensions. Two types of flux adjusters are used in this design: side adjusters, which bypass the magnet flux between two neighboring poles, and middle adjusters, which bypass the flux within a single pole between two V-shaped magnet segments. Figure 6.3B shows the concept at rest, and Figure 6.3C shows the final position of the flux adjusters in the slots after rotation.

This approach offers several advantages over other passive mechanical flux-reduction methods. Notably, it requires only a simple block of conducting material, unlike flux-blocking techniques that necessitate additional iron components, or magnet-repositioning strategies that demand precise displacement control. The optimal configuration, illustrated in Figure 6.3A, features two side holes positioned on either side of each magnet pair, along with a central hole located between the two magnets. Each hole accommodates an 8 mm flux adjuster element. An initial gap of 4 mm is provided to allow space for the unit cell responsible for the displacement. Additionally, a top gap clearance of 8 mm is allocated for the side holes, while the central hole is given a 5.5 mm gap to enable sufficient radial displacement of the block.

Using JMAG-FE, a multiphysics simulation software, our partner team at NRC simulated a wide range of dimensions and placements for the flux-adjuster holes and movable elements to identify the configuration that increases the most ω_{max1}, the maximum speed possible if no flux weakening is applied. These studies combine electromagnetic and mechanical models so that both flux reduction and the resulting stresses and strains in the rotor can be evaluated in parallel. The simulations test how the geometry of the adjusters, such as hole diameter, slot positioning, and displacement range, affected both air-gap flux linkage and rotor deformation at speed. The optimization process reveals clear trade-offs. Larger bypass holes or wider movers increase the ability to short-circuit magnet flux at high speed, but also weaken the rotor mechanically and risk excessive deformation. Conversely, smaller features preserve stiffness but have a limited flux-weakening effect. In the end, we identify a range of geometries that allowed meaningful flux reduction above the base speed while keeping stresses and strains within safe limits. For this proof of concept, a Toyota Prius motor is used as a reference model. However, the methodology is generalizable to any motor, provided its parameters are known.

Figure 6.4 shows the magnetic flux density in the motor at low speed (6297 rpm) and high speed (10428 rpm). By comparing Figure 6.4A, which shows the side adjusters at rest, with Figure 6.4B, where the same elements are displaced after their maximal displacement, a clear modification of the magnetic flux paths can be observed. In Figure 6.4A, most magnetic flux lines are directed toward the air gap and into the stator compared to Figure 6.4B where a portion of the flux is now directed towards the inner core of the rotor, reducing the amount of flux linking the stator. The reduction of flux is also seen when comparing the middle adjusters. Figure 6.4C shows the middle adjusters at rest and Figure 6.4D shows the same elements after maximal displacement. In Figure 6.4C, all the flux lines are going toward the air gap. In Figure 6.4D, after displacement, fewer lines are going to the stator as some is redirected toward the center of the rotor via the middle of the magnets. Those visual

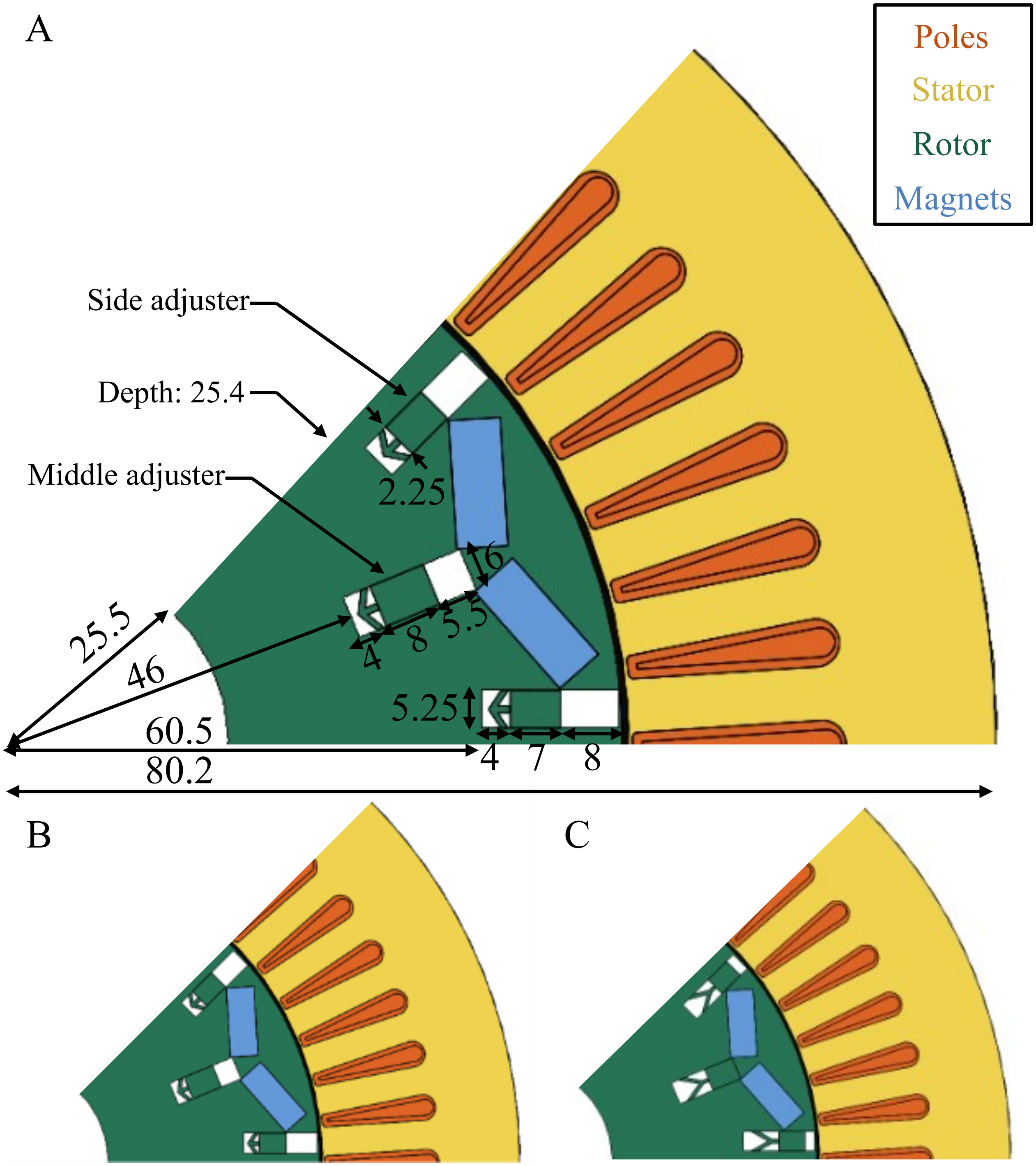

Figure 6.3 | **Concept to reduce the magnetic flux.** **(A)** The dimensions of the flux-adjuster holes and movable elements in the Toyota Prius rotor **(B)** At low speeds, the movable elements are closer to the center of the rotor **(C)** As the speed increases, the elements move towards the stator, which reduces the magnetic field in the rotor. All the dimensions are in mm.

differences of magnetic flux lines demonstrate that the proposed concept with the adjusters is effectively short-circuit part of the magnetic flux before it reaches the air gap which leads to a reduction of the flux linkage and enabling mechanical flux weakening.

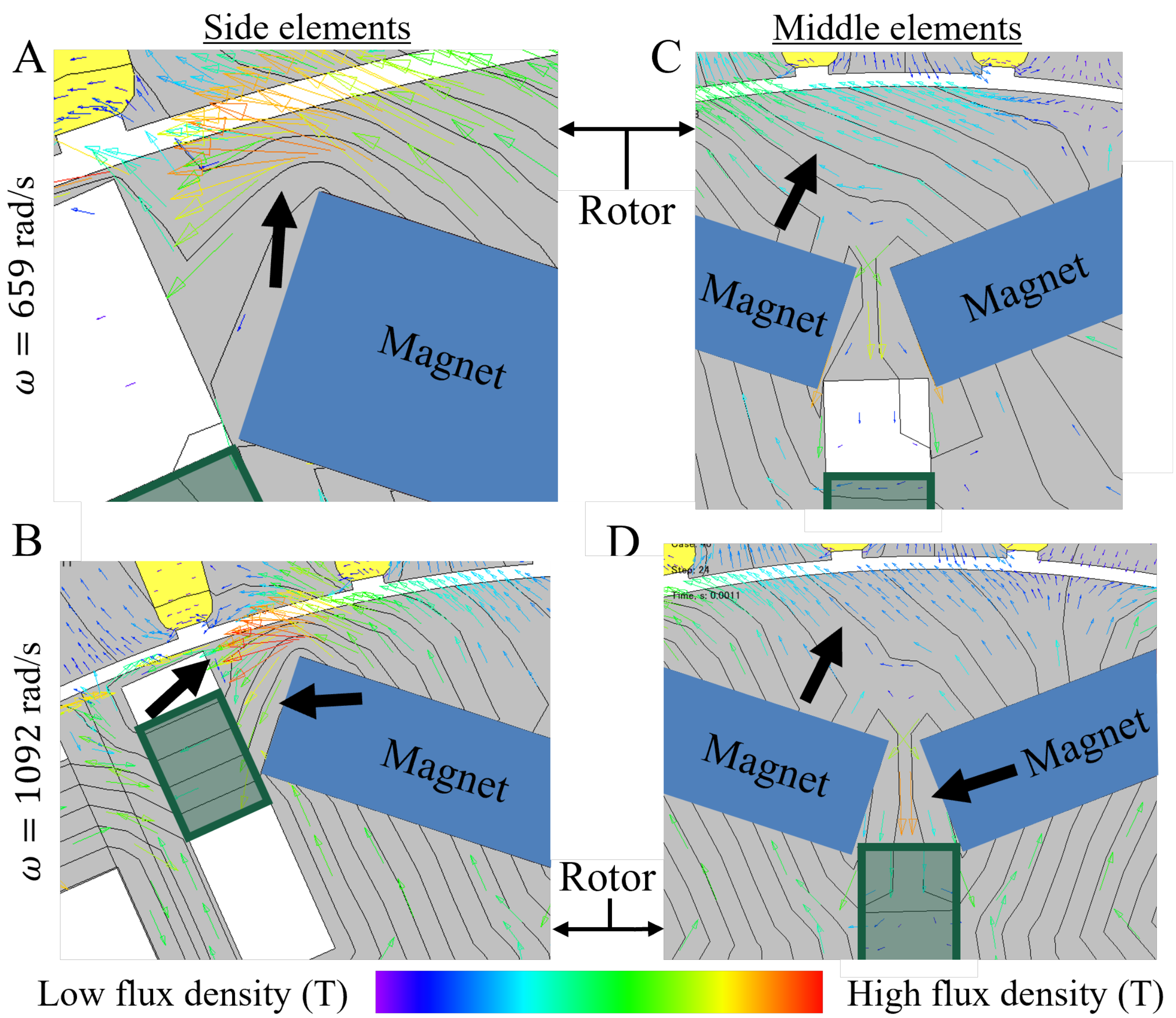

Figure 6.4 | **Concept to reduce the magnetic flux.** Representation of the magnetic flux density in a vector format **(A)** Side holes, low speeds: The magnetic flux is directed mostly towards the stator **(B)** Side holes, high speeds: The flux is now partly directed towards the center of the rotor via the element **(C)** Middle holes, low speeds: The magnetic flux is directed mostly towards the stator **(D)** Middle holes, high speeds: The flux is now partly directed towards the center of the rotor via the element between the magnets

6.4 Obtaining the optimal displacement curve based on the rotation to maximize torque

With the flux-weakening mechanism defined, the next step is to use JMAG FE to simulate the motor and determine the optimal variation of the flux linkage that maximizes the torque T. As shown in Figure 6.2, this process leads to a relationship between $\delta - \omega$ that can be programmed. The simulation operates by attempting to maximize the torque of the Toyota Prius modified with our proposed concept at each rotational speed. Initially, the adjusters are located at their initial positions inside the holes, near the center of the rotor as shown in Figure 6.3B. As the rotational speed increases, the required voltage also increases, eventually reaching the voltage limit at ω_{base}. Once the voltage limit is reached, the simulation progressively moves the middle and side adjusters toward the outer edge of the rotor, thereby decreasing the magnetic flux linkage. This reduction in flux helps maintain the voltage below its limit and allows the motor to sustain torque at higher speeds. This process is repeated as the rotational speed increases until the adjusters reach the end of the slots, as shown in Figure 6.3C, beyond which no more flux weakening can be achieved.

Figure 6.5 shows the behavior of the system. Figure 6.5A depicts the variation of the voltage, flux linkage and torque of our optimized concept. Torque is maximal and constant at low speeds, however, once the voltage hits its limit, maximum and non-zero torque at high speeds can only be achieved by maintaining a constant maximum voltage and minimizing the flux linkage as much as necessary. Knowing the optimal flux linkage variation, we can determine the optimal displacement of each flux adjuster element based on the motor's rotation. Figure 6.5B shows the optimal $\delta - \omega$ curve for the side and middle adjusters. Initially, both adjusters stay in their initial positions, as no flux reduction is required and any reduction would unnecessarily decrease torque. The results also indicate that the optimal flux weakening requires two different displacement-rotation curve for the side adjusters and the middle adjusters.

In Figure 6.5A, the voltage limit is reached around 400 rad/s, but the torque starts to decrease around 200 rad/s. However, in Figure 6.5B, the $\delta - \omega$ curves for both adjusters remain zero until 659 rad/s. This difference arises from the distinct definitions of the base speed ω_{base} for the Toyota Prius motor. The value of 659 rad/s corresponds to the base speed from a voltage-analysis standpoint, where the electrical voltage limit is reached and no more headroom against back-EMF is available, making flux weakening necessary. In contrast, at 200 rad/s corresponds to the base speed determined from the efficiency map of the motor and is related to the thermal and current limits during continuous operation. In this regime, the inverter limits the current in order to avoid overheating, leading to an earlier reduction in torque. This distinction also explains the change in the slope of the torque curve between

400-650 rad/s and 659-to the maximum speed.

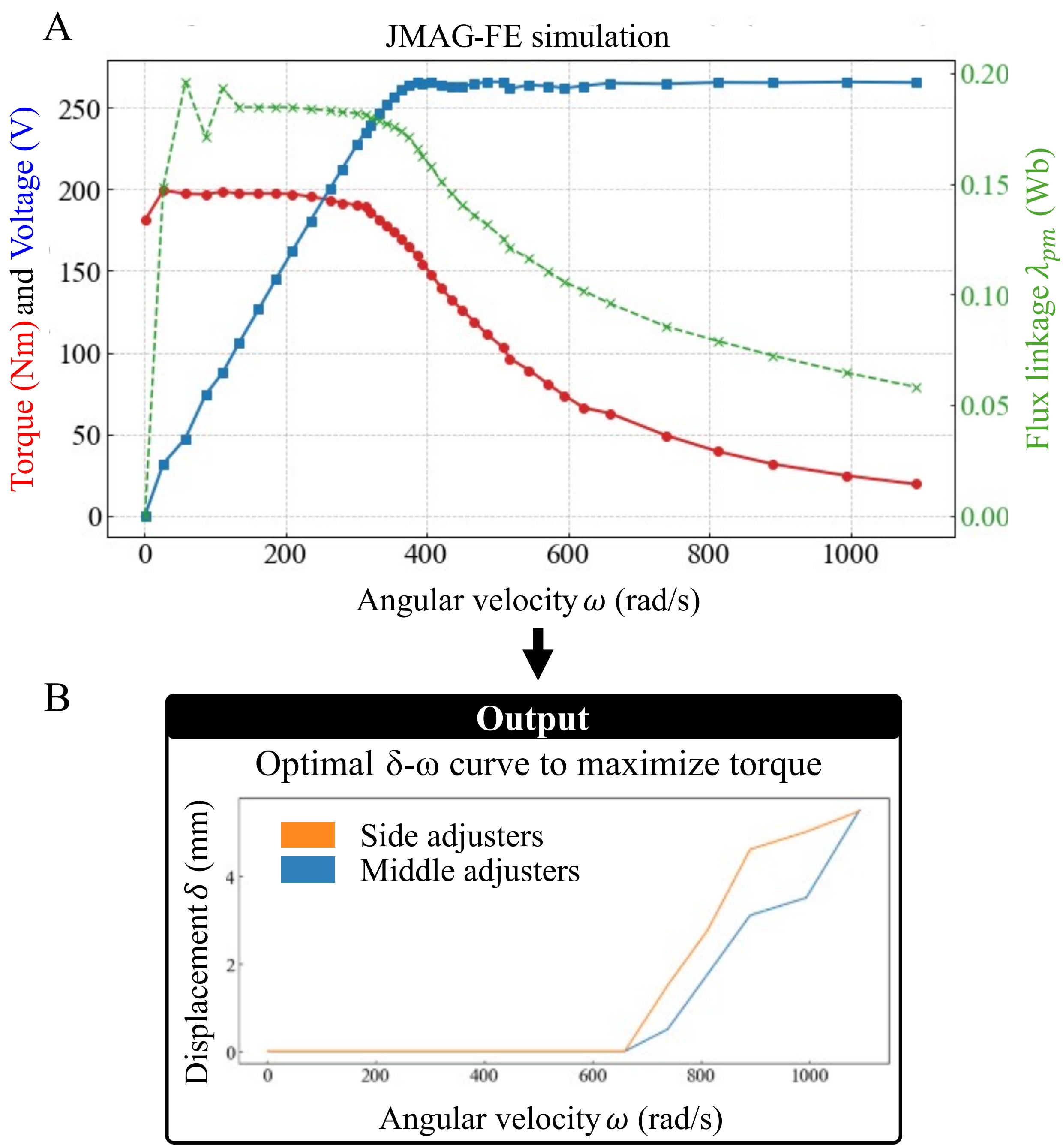

Figure 6.5 | **Evolution of the torque, voltage and flux linkage based on the rotation of the motor.** **(A)** The optimal flux reduction for maximum torque can be achieved by maximizing the voltage and reducing the flux linkage by the optimal amount **(B)** Optimal variation of the displacement for the adjusters in the middle and side holes based on the rotation speed (Output of the JMAG-FE simulation)

Although we aim to perform flux weakening using a purely mechanical approach, the proposed mechanism alone cannot provide sufficient flux reduction at higher speeds (beyond 994 rad/s), once the movers reach their maximum displacement and the voltage reaches its limit. To increase the performance and reach higher speeds, we incorporate a limited amount of electrical flux weakening beyond 994 rad/s. As a result, the current phase angle is slightly modified beyond this point. In a PMSM, the stator current is decomposed into two components, i_d and i_q. Modifying the current phase angle by injecting negative i_d reduces the flux linkage and helps limit the voltage, but the drawback is that it increases losses, as a larger portion of the current does not contribute to torque production and instead only generates additional heating. For this reason, the current phase angle should be kept as low as possible.

Using JMAG FE, we compare the performance of the proposed flux-weakening solution with that of a purely electrical flux-weakening solution. Table 6.1 shows a comparison between the two solutions and Figure 6.6 shows the torque-speed curves of each solution. The purely electrical flux-weakening solution can reduce the flux linkage by 53%, however, the torque quickly drops after 994 rad/s, reaching near zero at 1092 rad/s. In comparison, the combined mechanical flux-weakening and electrical flux-weakening solution can reduce the flux linkage by 40%, while the torque only decreases by 69% at the same speed. As a result, the motor is able to maintain sufficient torque at higher speeds, which is not possible with pure electrical flux weakening. Another advantage of the proposed flux-weakening method is that the current phase angle remains lower at high speeds compared to the pure electrical flux-weakening solution which becomes 89 degrees. This large phase angle induces a lot of current-related losses. Thus, our proposed solution offers better efficiency, defined as the ratio of mechanical output power to electrical input power, for comparable torque and power values across a wider speed range (0-1092 rad/s) compared to pure electrical flux weakening, as shown in Table 6.1.

Speed (rad/s)	**Phase angle (°)**		**Torque (Nm)**		**Efficiency (%)**	
	Proposed	Pure Elec.	Proposed FW	Pure Elec.	Proposed	Pure Elec.
659	60	61	62.63	66.56	95.93	95.61
738	60	64	49.16	51.01	95.66	95.24
812	60	66	39.32	38.70	95.29	94.80
891	60	70	31.46	27.12	94.49	94.42
994	64	78.4	24.45	13.71	93.58	92.12
1092	65.6	89	19.23	0.12	92.56	11.92

Table 6.1 | **Comparison between the proposed solution versus a pure electrical flux-weakening solution.** Comparison between the current angle phase, the torque and the efficiency of our proposed solution versus a pure electrical flux-weakening solution

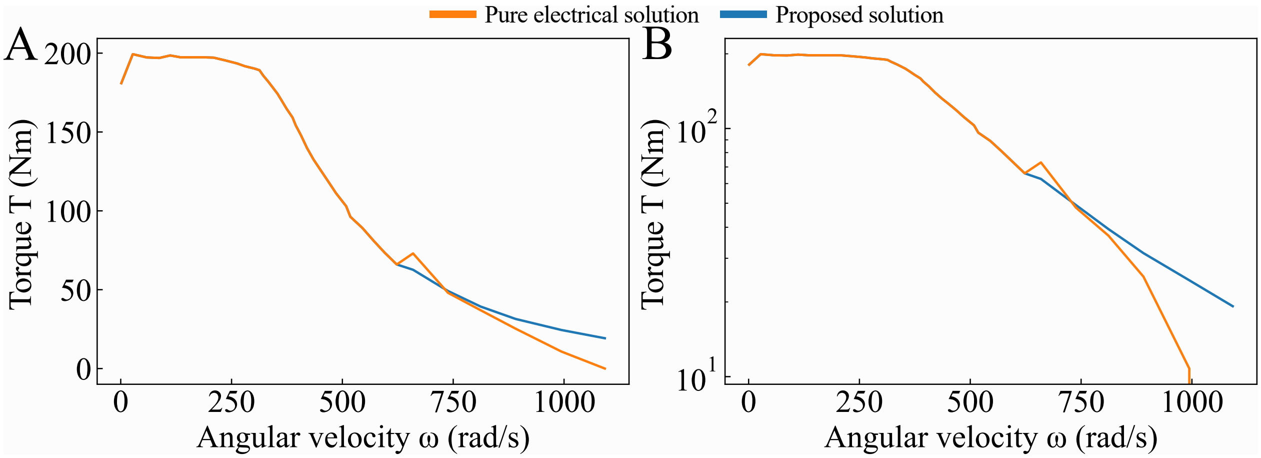

Figure 6.6 | **Comparison of torque based on speed for our proposed solution and pure electrical solution.** **(A)** Comparison of the evolution of the torque based on the rotation of the motor for the proposed flux-weakening solution that combines mechanical and electric flux-weakening (FW) and a pure electrical flux-weakening solution **(B)** Same comparison but with a log axis. All the results are output of the JMAG-FE simulation

6.5 Inverse design unit cell parameters to program the displacement-rotation curves

With the desired displacement-rotation curves defined in Section 6.4 and shown in Figure 6.5B for both adjusters, we can now find the parameters for the unit cells that give the most fitting displacement-rotation curve. Figure 6.7 shows a comparison for both the side and middle adjusters, the optimal $\delta - \omega$ curves obtained from JMAG FE simulations and the most fitting curve of the unit cell selected by the algorithm of inverse design in Figure 6.1. We use Somaloy 700HR 3P for the block material from Höganäs. This material can be 3D printed and can conduct flux. The density of this material is 7.4 g/cm^3 [58]. For the von Mises truss, a flexible material is required. We impose an arbitrary constraint on the Young's modulus, ranging from 400 to 500 MPa, to identify an optimal value. We also assume a density of 1.2 g/cm^3. These values are representative of available thermoplastic polyurethane (TPU) materials and correspond to the mid-range of Young's modulus for TPU, which spans approximately 10 to 1000 MPa depending on hardness [59, 60]. These values can be adjusted once the the manufacturing process of the rotor is defined. Additionally, flexible materials with higher Young's modulus could be considered. Therefore, this range is primarily arbitrary and serves as a proof of concept. We assume a neo-Hookean hyperelastic incompressible material to use the database obtained in Section 4.2.

Figure 6.7A shows the optimal curve obtained with our unit cell for the middle movers, and Figure 6.7B shows the optimal curve obtained with our unit cell for the side movers. While the overall trend between the target and the output curves is respected in both cases, the final displacement occurs at a higher rpm. This discrepancy can be explained by the reduced design space imposed by application constraints. In particular, the ratio of required displacement by the mechanism to available width exceeds 0.9 in both cases. Assuming the maximum unit cell displacement is limited to $2a$, it implies that $\frac{a}{l} > 0.45$. Based on the design space obtained in Section 4.2 and presented in Figure 4.2C, the only possible geometries are in the snap or bistable families. However, bistable configurations must be excluded, as the mechanism is required to return to its original position when the motor speed decreases. These constraints significantly limit the available design options. In Figure 6.7, larger displacements than $2a$ are permitted to improve performance and further explore the available design space.

To obtain results more tailored to the application, we need to increase the design space. One way to achieve this is by stacking unit cells on top of each other. By doing so, we can reduce the displacement required for each unit cell and possibly combine multiple families to obtain a more customized response. Here, we assume a theoretical perfect stacking. In reality, stacking requires modifications to the geometry of the von Mises truss in order to combine them. Figure 6.7C shows the optimal curve obtained with two unit cells for the middle movers, and Figure 6.7D shows the optimal curve obtained with two unit cells for the side movers. We observe a better agreement between the two curves with this configuration. A small issue of stacking is that it takes more vertical space to accommodate in the rotor, exceeding a bit the height envelope, however it does not have a significant impact on the motor performance at high speeds. For instance, increasing this vertical space to 5 or 6 mm results in a slight reduction in performance of flux weakening, while the torque remains unchanged. Another way to expand the design space is to increase the width l of the unit cell. However, in this case, increasing the width of the rotor hole reduces the effectiveness of the proposed mechanical flux-weakening solution, and, consequently, the motor performance at high speeds.

These results show that the use of unit cells in a rotor to achieve mechanical flux-weakening is feasible. They also demonstrate the versatility of the unit cell in an application, as it can produce a tailored response to match a target curve using appropriate materials for the given use case.

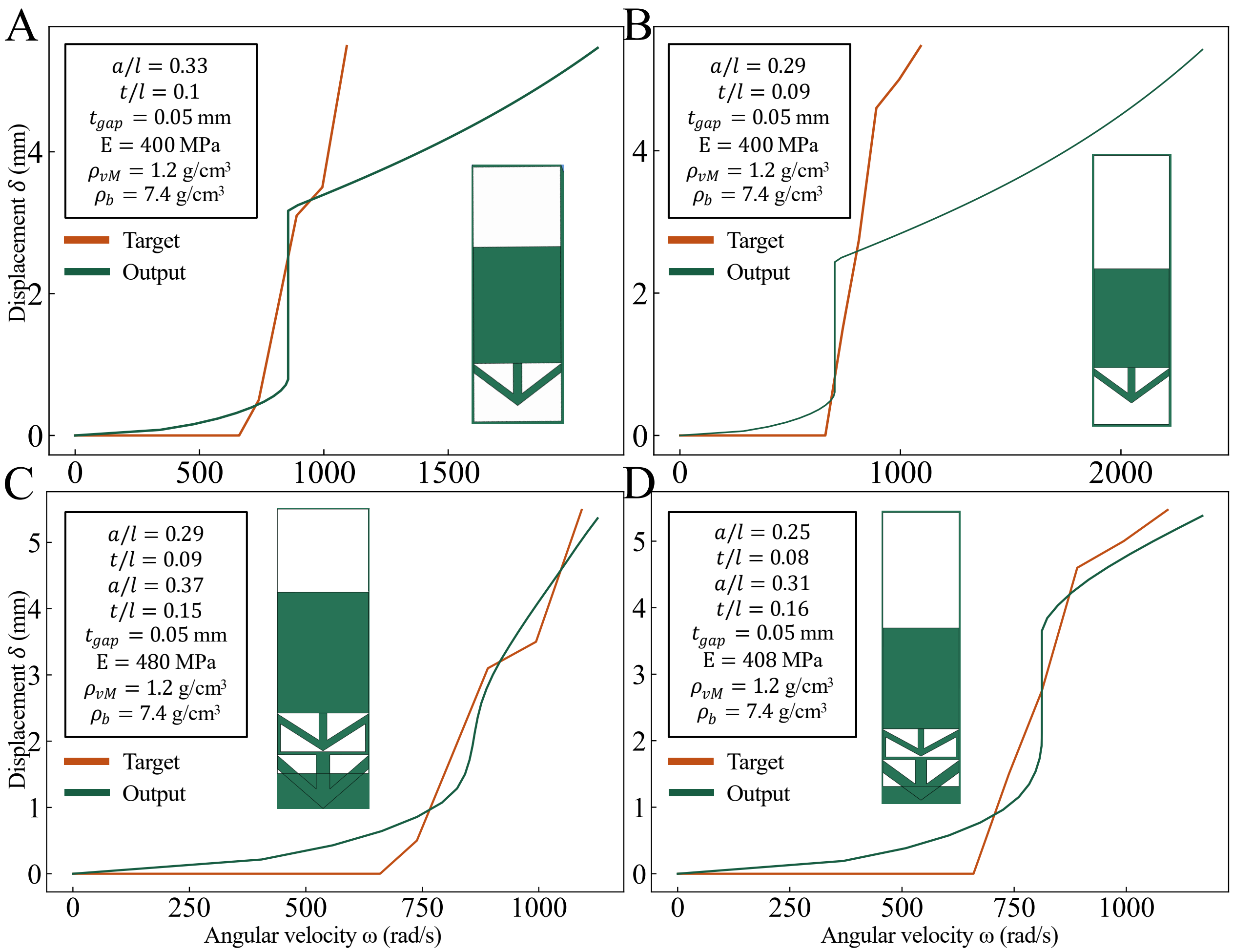

Figure 6.7 | **Comparison for both the side and middle adjusters, the optimal $\delta - \omega$ curves obtained from JMAG FE simulations and the most fitting curve of the unit cell selected by the Python algorithm of inverse design.** **(A)** Middle movers (Single unit cell) **(B)** Side movers (Single unit cell) **(C)** Middle movers (Double unit cells) **(D)** Side movers (Double unit cells)

CHAPTER 7 CONCLUSION

7.1 Summary of contributions

In this thesis, we introduced a centrifugal-force-driven mechanical metamaterial unit cell whose deformation can be programmed to obtain any displacement-rotation curve. The structure uses a von Mises truss coupled to a block to produce a geometry with nonlinear deformation. FE simulations revealed four types of response: (1) monotonic, (2) transient, (3) snap and (4) bistable. The response is primarily governed by geometric ratios like $\frac{a}{l}$ and $\frac{t}{l}$. These numerical observations were validated experimentally using silicone molded samples with tensile tests to confirm static FE simulations and with a custom-built test bench to validate dynamic FE simulations. The experimental results were in good agreement with the simulation results, and are consistent with the ones presented in the literature.

We also showed that it was possible to predict the displacement-rotation curve ($\delta - \omega$) directly from the static force-displacement ($F - \delta$) curve using the centrifugal force relation. This technique allows the possibility to quickly obtain the dynamic behavior of any structure without running computationally expensive simulations. There was a good agreement between the predicted curves for the four types of response and the dynamic FE simulations performed.

This thesis also introduced an inverse-design method to find a unit cell that has a deformation that matches any wanted deformation based on the rotation. A Python script uses all the static $F - \delta$ curves obtained for all the different geometric unit cell parameters and selects the unit cell parameters that most closely matched the wanted curve, while taking into account the user constraints like the radial location and the available envelope.

Finally, in collaboration with the NRC, we proposed a passive mechanical flux weakening concept for IPMSMs based on the Toyota Prius motor that uses side and middle flux-adjuster elements to short-circuit magnetic flux. Using JMAG-FE simulations, optimal displacement of the mechanism in rotation was obtained. Using the inverse-design method, we found unit cells that reproduced closely the wanted displacement-rotation curve for optimal performance of the motor. With our proposed solution, the torque only decreases by 69% at high speeds (around 10 000 rpm) compared to nearly zero for a purely electrical flux-weakening solution, allowing the motor to operate at enough torque at higher speeds. This concept paves the way for future high-speed meta-motors for aerospace applications, capable of operating at rotational speeds exceeding 30 000 rpm.

7.2 Limitations and future research

Several limitations could be addressed based on the presented work in this thesis and could be addressed in future work.

The utilization of silicone for the experimentation was used for its reproducibility, ease of fabrication, anisotropy and suitability for large deformations. Additionally, for the flexible part of the structure, material properties representative of TPU were used in the inverse design as part of the proof of concept for the proposed mechanical flux-weakening solution. However, for an application like in an electric motor, other materials should be explored. Since the goal is to develop a rotor for a high-speed motor, the chosen material must exhibit high stiffness. Moreover, it must possess compatible electrical, magnetic, mechanical, and thermal properties. These stringent requirements significantly limit the types of AM technologies that can be used. Two materials could be options considering all the requirements: magnetic materials like soft magnetic composite (SMC) [61] and fiber-metal [62]. Several additive manufacturing techniques can be considered for printing these materials, each with its own advantages and limitations: (1) Cold spray technique [61, 63, 64], (2) Laser Powder Bed Fusion (LPBF) [65, 66], (3) FFF [67].

Furthermore, in the application process, some constraints were not considered for finding the optimal possible unit cell, such as the magnetic force applied on the adjusters during rotation. In a motor, these forces vary with the radial position and thus it can influence the deformation curve of the unit cell. Also, if the magnetic force exceeds the restoring force of the metamaterial structure, the mechanism may remain deployed even after the rotation speed decreases. Also, we did not consider the potential hysteresis of the chosen configurations. Those constraints are key elements that should be studied for an application like in a PMSM motor.

We also demonstrated that the output curve can be more closely tailored to the target curve by theoretically stacking more than one unit cell. The real geometry of such a stacked structure should be studied to better understand the behavior of a stacked unit, as the geometry of the structure needs to be adapted to accommodate the combination of two or more von Mises trusses.

The long term potential of this work could be significant because this kind of mechanism could be implemented in electric motors to make transportation greener and more cost-effective.

APPENDIX A MESH CONVERGENCE ANALYSIS

This appendix describes the mesh convergence study performed on the unit cell truss with a width $l = 20$, $\frac{a}{l} = 0.2$ and $\frac{t}{l} = 0.1$ under the static tensile setup described in Section 4.2. Plane-stress quadratic elements (CPS6) in Abaqus are used. We measure and compare the last value of the reaction force $RF2$ after a displacement $\delta = 2 \cdot a$ is imposed.

To quantify convergence, we use the solution at the coarsest mesh ($h = 1$) as the initial reference $RF2$. The relative variation (%) for each subsequent element size h is defined as $\Delta(\%) = |\frac{RF_i - RF_{i-1}}{RF_{i-1}}| \cdot 100$ where RF_i is the reaction force for the mesh with element size h_i. A tolerance of $\Delta < 0.1\%$ is used as the acceptance criterion for mesh independence.

The table A.1 shows the relative variation of each element size from 1.0 to 0.1 . As the element size reduces, the relative variation reduces to reach 0.1% at $h = 0.5$ and then stabilize. Therefore, $h = 0.5$ is selected for the production meshes, balancing accuracy and computational cost.

Table A.1 | **Mesh convergence analysis.** Mesh convergence for the static tensile case $l = 20$, $\frac{a}{l} = 0.2$ and $\frac{t}{l} = 0.1$. Plane stress elements (CPS6) in Abaqus.

Element Size (h)	Reaction Force RF2 (N)	Relative Variation (%)
1.0	(Initial Value)	-
0.9	2.738729	0.17 %
0.8	2.727006	0.43 %
0.7	2.723908	0.11 %
0.6	2.717976	0.22 %
0.5	**2.715224**	**0.10** %
0.4	2.712560	0.10 %
0.3	2.708663	0.14 %
0.2	2.706313	0.09 %
0.1	2.704216	0.08 %

APPENDIX B ELECTRICAL CONNECTIONS

Figure B.1 shows the electrical connections of the test bench presented in Section 5.3. These connections link all active components of the setup: the power supply, the DC motor, the Hall-effect sensor, and the Arduino microcontroller.

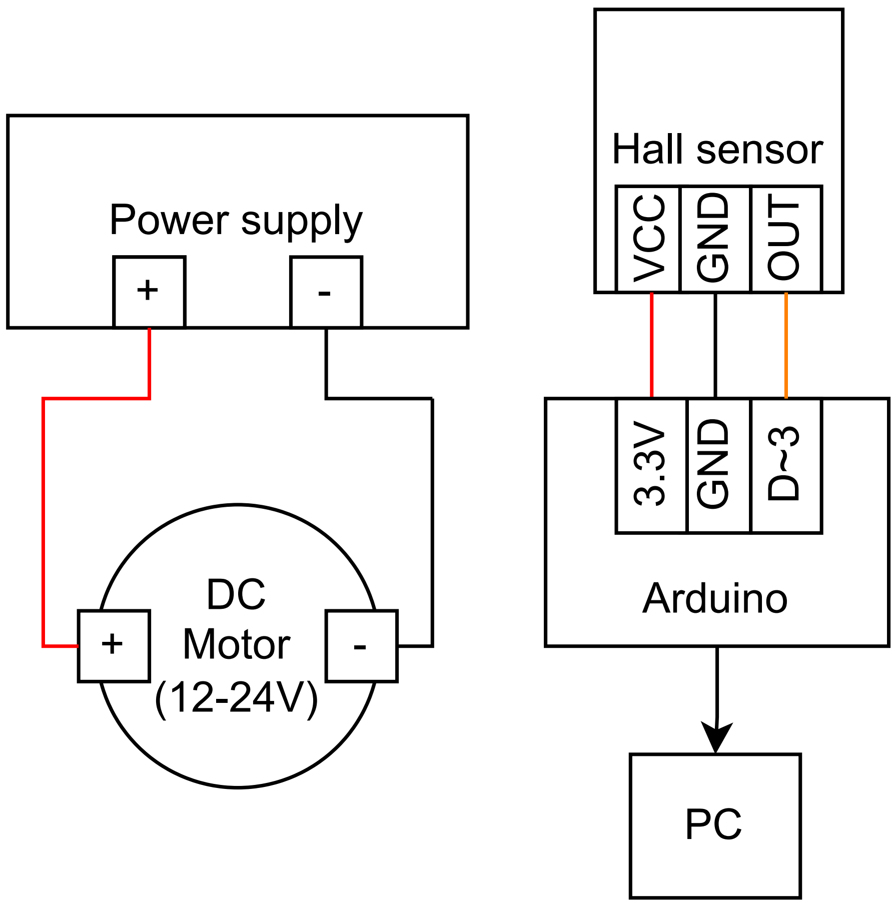

Figure B.1 | **Electric connections of the test bench.** The DC motor is connected to a power supply. A Hall-effect sensor is connected to an Arduino to measure the actual rotational speed of the arm in real time, which is transmitted to the connected PC.

APPENDIX C ELECTRIC MOTORS

In this Appendix, we dive deeper on flux-weakening and the governing PMSM equations.

When the motor begins to rotate, ω, the angular rotation of the rotor increases, it operates in the Constant Torque Speed Region (CTSR). In this region, the torque delivered by the motor is both constant and maximal. The voltage of the stator in an IPMSM is defined as:

$$u_s = \sqrt{(\omega L_q i_q)^2 + (\omega(\lambda_{pm} + L_d i_d))^2} \tag{C.1}$$

λ_{pm} represents the flux linkage produced by the rotor PMs, L_q and L_d are direct axis (d-axis) and quadrature-axis (q-axis) inductances, and i_q and i_d are direct axis (d-axis) and quadrature-axis (q-axis) stator currents. i_q and i_d can weaken or strengthen the effective air-gap flux, and produce the main electromagnetic torque, respectively. For an IPM motor, the electromagnetic torque is:

$$T_e = \frac{3}{2} p(\lambda_{pm} i_q + (L_d - L_q) i_d i_q) \tag{C.2}$$

The parameters in this equation, L_d and L_q, are motor-specific parameters and are constant. The first term ($\lambda_{pm} i_q$) represents the magnet torque and the second term $(L_d - L_q) i_d i_q$ represents the reluctance torque. Note that this reluctance torque is only present in IPM, not in Surface Permanent Magnet (SPM) which are another type of PMSMs.

In the CTSR region, λ_{pm}, i_q and i_d are constant.

However, as the rotational speed increases, back-EMF also increases. We know that:

$$u_s \leq u_{max} \tag{C.3}$$

where u_{max} is the maximum voltage that the inverter can supply. Therefore, we can calculate the rpm (or ω_{base}) at which $u_s = u_{max}$. After rearranging the equation in C.1, we obtain:

$$\omega_e = \sqrt{\frac{u_{max}^2}{(L_q * i_q)^2 + (L_d * i_d + \lambda_{pm})^2}} \tag{C.4}$$

This means that if no adjustments are made, at ω_{base}, the voltage will reach its maximum, and the torque will quickly decrease. The reason for this is that the back-EMF continues to increase with speed, but the voltage cannot compensate beyond the inverter's maximum limit.

To increase ω_{max1}, which represents the maximum ω before the torque reaches zero, and widen the operational range of the PMSM, we need to revisit equation C.1. There are two potential solutions: **1)** inserting negative d-axis current by increasing the current phase angle, thereby reducing the value of λ_{pm} **2)** reducing mechanically the value of λ_{pm} These modifications are referred to as "Flux-weakening" [68]. Flux-weakening is a technique that enables the motor to operate at higher speeds while delivering maximum torque per current given available voltage This is why the region reached at higher rpm, more precisely, at ω_{base}, depending on the motor's parameters, is called the Constant Power Region (CPSR). In this region, the voltage is at its maximum and remains constant. Note that gears are not used to artificially increase the maximum torque or speed range, as adding gears would complicate the system unnecessarily which will add weights and rise costs, and add more source of failure to the motor. [12]

The most common method to implement flux weakening is through control algorithms that shift the current angle by injecting negative i_d, thereby counteracting the PM flux and enabling operation above base speed. This method is called "Electrical flux weakening". In this process, i_q is still regulated independently to produce torque, typically chosen to maximize torque per ampere while ensuring that thermal and loss constraints remain manageable. However, the drawbacks of this method include reduced efficiency, increased cost and complexity and difficulty in implementation [12].

The alternative solution to electrical flux weakening (FW), would be to use a mechanical design approach to achieve flux weakening. This method is called "Mechanical flux weakening". For instance, specific rotor geometries, such as varying the position of the PMs, shaping flux barriers, or creating bypass flux paths, allow some of the magnet flux to return through the rotor rather than passing entirely through the stator. This structural design inherently reduces the effective air-gap flux at high speed. Besides, it is possible to employ mechanical devices known as flux adjuster elements (FAEs), which physically modify the magnet flux. These FAEs can be self-actuated (responding passively to centrifugal forces or magnetic saturation) or actively controlled by auxiliary actuators. By incorporating such mechanisms, the PMSM can further extend its operating speed range, reaching a higher maximum speed ω_{max2}, without injecting significant i_d current, thereby eliminating or minimizing losses associated with this negative current.

However, changing the value of λ_{pm} not only affects the stator voltage but also the torque of the motor.

From equation C.2, it is evident that the electromagnetic torque has a direct dependence on the permanent magnet flux linkage λ_{pm}. Therefore, changing λ_{pm} significantly influences motor performance. While a higher λ_{pm} increases torque capability at low and medium speeds, it also raises back-EMF, which limits high-speed operation. Conversely, reducing λ_{pm} lowers the available torque but enables an extended constant-power speed range. Simulation software such as JMAG-Designer (FE analysis) can be used to model these trade-offs, allowing rotor design optimization to balance torque density with high-speed performance.

REFERENCES

[1] C. Jiang, F. Rist, H. Wang, J. Wallner, and H. Pottmann, “Shape-morphing mechanical metamaterials,” *Computer-Aided Design*, vol. 143, p. 103146, Feb. 2022. [Online]. Available: http://dx.doi.org/10.1016/j.cad.2021.103146

[2] L. Virgin, “On the elastic snapping of structural elements,” *International Journal of Non-Linear Mechanics*, vol. 149, p. 104329, Mar. 2023. [Online]. Available: http://dx.doi.org/10.1016/j.ijnonlinmec.2022.104329

[3] A. Iniguez-Rabago, Y. Li, and J. T. B. Overvelde, “Exploring multistability in prismatic metamaterials through local actuation,” *Nature Communications*, vol. 10, no. 1, Dec. 2019. [Online]. Available: http://dx.doi.org/10.1038/s41467-019-13319-7

[4] S. Shan, S. H. Kang, J. R. Raney, P. Wang, L. Fang, F. Candido, J. A. Lewis, and K. Bertoldi, “Multistable architected materials for trapping elastic strain energy,” *Advanced Materials*, vol. 27, no. 29, p. 4296–4301, Jun. 2015. [Online]. Available: http://dx.doi.org/10.1002/adma.201501708

[5] B. Gorissen, D. Melancon, N. Vasios, M. Torbati, and K. Bertoldi, “Inflatable soft jumper inspired by shell snapping,” *Science Robotics*, vol. 5, no. 42, May 2020. [Online]. Available: http://dx.doi.org/10.1126/scirobotics.abb1967

[6] Y. Zhang, W. Z. Jiang, Y. Pan, X. C. Teng, H. H. Xu, H. Yan, X. H. Ni, J. Dong, D. Han, W. Q. Chen, J. Yang, Y. M. Xie, Y. Lu, and X. Ren, “Temperature-responsive metamaterials made of highly sensitive thermostat metal strips,” *Science Advances*, vol. 10, no. 49, Dec. 2024. [Online]. Available: http://dx.doi.org/10.1126/sciadv.ads0892

[7] E. Gutierrez-Prieto, M. Gomez, and P. M. Reis, “Harnessing centrifugal and euler forces for tunable buckling of a rotating elastica,” *Extreme Mechanics Letters*, vol. 72, p. 102246, Nov. 2024. [Online]. Available: http://dx.doi.org/10.1016/j.eml.2024.102246

[8] Y. Zhang, X. Zhang, T. Qian, and R. Hu, “Modeling and simulation of a passive variable inertia flywheel for diesel generator,” *Energy Reports*, vol. 6, p. 58–68, Dec. 2020. [Online]. Available: http://dx.doi.org/10.1016/j.egyr.2020.01.001

[9] E. Agamloh, A. von Jouanne, and A. Yokochi, “An overview of electric machine trends in modern electric vehicles,” vol. 8, no. 2, p. 20, 2020. [Online]. Available: https://www.mdpi.com/2075-1702/8/2/20

[10] J.-M. Mun, G.-J. Park, S. Seo, D.-W. kim, Y.-J. Kim, and S.-Y. Jung, "Design characteristics of IPMSM with wide constant power speed range for EV traction," vol. 53, no. 6, pp. 1–4, 2017. [Online]. Available: https://ieeexplore.ieee.org/document/7843585

[11] J. Cekani, F. G. Capponi, G. De Donato, and F. Caricchi, "Mechanical flux weakening methods for the achievement of a very wide constant power speed range in automotive applications," vol. 10, no. 3, pp. 3443–3458, 2022. [Online]. Available: https://ieeexplore.ieee.org/document/9350658/

[12] N. Bianchi, P. G. Carlet, L. Cinti, and L. Ortombina, "A review about flux-weakening operating limits and control techniques for synchronous motor drives," *Energies*, vol. 15, no. 5, p. 1930, Mar. 2022. [Online]. Available: http://dx.doi.org/10.3390/en15051930

[13] A. A. Zadpoor, "Mechanical meta-materials," *Materials Horizons*, vol. 3, no. 5, p. 371–381, 2016. [Online]. Available: http://dx.doi.org/10.1039/C6MH00065G

[14] X. Yu, J. Zhou, H. Liang, Z. Jiang, and L. Wu, "Mechanical metamaterials associated with stiffness, rigidity and compressibility: A brief review," *Progress in Materials Science*, vol. 94, pp. 114–173, May 2018. [Online]. Available: http://dx.doi.org/10.1016/j.pmatsci.2017.12.003

[15] J. Huang, J. Zhang, D. Xu, S. Zhang, H. Tong, and N. Xu, "From jammed solids to mechanical metamaterials: A brief review," *Current Opinion in Solid State and Materials Science*, vol. 27, no. 1, p. 101053, Feb. 2023. [Online]. Available: http://dx.doi.org/10.1016/j.cossms.2022.101053

[16] S. Tu, X. Ren, J. He, and Z. Zhang, "Stress–strain curves of metallic materials and post-necking strain hardening characterization: A review," *Fatigue amp; Fracture of Engineering Materials amp; Structures*, vol. 43, no. 1, p. 3–19, Oct. 2019. [Online]. Available: http://dx.doi.org/10.1111/ffe.13134

[17] B. I. Oladapo, S. O. Ismail, O. M. Ikumapayi, and P. G. Karagiannidis, "Impact of rgo-coated peek and lattice on bone implant," *Colloids and Surfaces B: Biointerfaces*, vol. 216, p. 112583, Aug. 2022. [Online]. Available: http://dx.doi.org/10.1016/j.colsurfb.2022.112583

[18] A. Almesmari, N. Baghous, C. J. Ejeh, I. Barsoum, and R. K. Abu Al-Rub, "Review of additively manufactured polymeric metamaterials: Design, fabrication, testing and modeling," *Polymers*, vol. 15, no. 19, p. 3858, Sep. 2023. [Online]. Available: http://dx.doi.org/10.3390/polym15193858

[19] C. Liu, X. Zhang, J. Chang, Y. Lyu, J. Zhao, and S. Qiu, “Programmable mechanical metamaterials: basic concepts, types, construction strategies—a review,” *Frontiers in Materials*, vol. 11, Mar. 2024. [Online]. Available: http://dx.doi.org/10.3389/fmats.2024.1361408

[20] A. Rafsanjani, A. Akbarzadeh, and D. Pasini, “Snapping mechanical metamaterials under tension,” *Advanced Materials*, vol. 27, no. 39, p. 5931–5935, Aug. 2015. [Online]. Available: http://dx.doi.org/10.1002/adma.201502809

[21] N. Khan and A. Riccio, “A systematic review of design for additive manufacturing of aerospace lattice structures: Current trends and future directions,” *Progress in Aerospace Sciences*, vol. 149, p. 101021, Aug. 2024. [Online]. Available: http://dx.doi.org/10.1016/j.paerosci.2024.101021

[22] S. Chen, B. Wang, S. Zhu, X. Tan, J. Hu, X. Lian, L. Wang, and L. Wu, “A novel composite negative stiffness structure for recoverable trapping energy,” *Composites Part A: Applied Science and Manufacturing*, vol. 129, p. 105697, Feb. 2020. [Online]. Available: http://dx.doi.org/10.1016/j.compositesa.2019.105697

[23] S. Kamrava, R. Ghosh, Z. Wang, and A. Vaziri, “Origami-inspired cellular metamaterial with anisotropic multi-stability,” *Advanced Engineering Materials*, vol. 21, no. 2, Oct. 2018. [Online]. Available: http://dx.doi.org/10.1002/adem.201800895

[24] W. Liu, Y. Zhang, Z. Guo, D. Li, S. Zhao, and W. Xie, “Analyzing in-plane mechanics of a novel honeycomb structure with zero poisson’s ratio,” *Thin-Walled Structures*, vol. 192, p. 111134, Nov. 2023. [Online]. Available: http://dx.doi.org/10.1016/j.tws.2023.111134

[25] H. Wang, D. Zhao, Y. Jin, M. Wang, T. Mukhopadhyay, and Z. You, “Modulation of multi-directional auxeticity in hybrid origami metamaterials,” *Applied Materials Today*, vol. 20, p. 100715, Sep. 2020. [Online]. Available: http://dx.doi.org/10.1016/j.apmt.2020.100715

[26] Y. Liétard, D. Therriault, and D. Melancon, “Exploiting geometric frustration in coupled von mises trusses to program multifunctional mechanical metamaterials,” *Advanced Engineering Materials*, vol. 27, no. 11, Jun. 2025. [Online]. Available: http://dx.doi.org/10.1002/adem.202570037

[27] Z. Zhai, Y. Wang, and H. Jiang, “Origami-inspired, on-demand deployable and collapsible mechanical metamaterials with tunable stiffness,” *Proceedings of the National*

Academy of Sciences, vol. 115, no. 9, p. 2032–2037, Feb. 2018. [Online]. Available: http://dx.doi.org/10.1073/pnas.1720171115

[28] F. O. Falope, M. Pelliciari, L. Lanzoni, and A. M. Tarantino, "Snap-through and eulerian buckling of the bi-stable von mises truss in nonlinear elasticity: A theoretical, numerical and experimental investigation," *International Journal of Non-Linear Mechanics*, vol. 134, p. 103739, Sep. 2021. [Online]. Available: http://dx.doi.org/10.1016/j.ijnonlinmec.2021.103739

[29] H. Zhang, J. Wu, D. Fang, and Y. Zhang, "Hierarchical mechanical metamaterials built with scalable tristable elements for ternary logic operation and amplitude modulation," *Science Advances*, vol. 7, no. 9, Feb. 2021. [Online]. Available: http://dx.doi.org/10.1126/sciadv.abf1966

[30] K. Bertoldi, V. Vitelli, J. Christensen, and M. van Hecke, "Flexible mechanical metamaterials," *Nature Reviews Materials*, vol. 2, no. 11, Oct. 2017. [Online]. Available: http://dx.doi.org/10.1038/natrevmats.2017.66

[31] N. Bastola, J. Ma, and M. P. Jahan, "Design and numerical investigation of the 3d reinforced re-entrant auxetic and hexagonal lattice structures for energy absorption properties," *Manufacturing Letters*, vol. 41, p. 1100–1108, Oct. 2024. [Online]. Available: http://dx.doi.org/10.1016/j.mfglet.2024.09.135

[32] J. T. Overvelde, T. A. de Jong, Y. Shevchenko, S. A. Becerra, G. M. Whitesides, J. C. Weaver, C. Hoberman, and K. Bertoldi, "A three-dimensional actuated origami-inspired transformable metamaterial with multiple degrees of freedom," *Nature Communications*, vol. 7, no. 1, Mar. 2016. [Online]. Available: http://dx.doi.org/10.1038/ncomms10929

[33] R. Xu, C. Chen, J. Sun, Y. He, X. Li, M.-H. Lu, and Y. Chen, "The design, manufacture and application of multistable mechanical metamaterials-a state-of-the-art review," *International Journal of Extreme Manufacturing*, vol. 5, no. 4, p. 042013, Oct. 2023. [Online]. Available: http://dx.doi.org/10.1088/2631-7990/acf96a

[34] R. Gautam, S. Idapalapati, and S. Feih, "Printing and characterisation of kagome lattice structures by fused deposition modelling," *Materials amp; Design*, vol. 137, p. 266–275, Jan. 2018. [Online]. Available: http://dx.doi.org/10.1016/j.matdes.2017.10.022

[35] B. G. Compton and J. A. Lewis, "3d-printing of lightweight cellular composites," *Advanced Materials*, vol. 26, no. 34, p. 5930–5935, Jun. 2014. [Online]. Available: http://dx.doi.org/10.1002/adma.201401804

[36] L. Wang, Y. Chang, S. Wu, R. R. Zhao, and W. Chen, “Physics-aware differentiable design of magnetically actuated kirigami for shape morphing,” *Nature Communications*, vol. 14, no. 1, Dec. 2023. [Online]. Available: http://dx.doi.org/10.1038/s41467-023-44303-x

[37] K. Barvenik, M. Bonthron, A. Jones, and E. Tubaldi, “Soft porous metamaterials using inflation-induced buckling for smart actuation,” *Nature Communications*, vol. 16, no. 1, Aug. 2025. [Online]. Available: http://dx.doi.org/10.1038/s41467-025-63072-3

[38] E. Gutierrez-Prieto, C. M. Meulblok, M. van Hecke, and P. M. Reis, “Dynamic driving enables independent control of material bits for targeted memory,” 2025. [Online]. Available: https://arxiv.org/abs/2508.16257

[39] D. Wang, H. Xu, J. Wang, C. Jiang, X. Zhu, Q. Ge, and G. Gu, “Design of 3d printed programmable horseshoe lattice structures based on a phase-evolution model,” *ACS Appl. Mater. Interfaces*, vol. 12, no. 19, pp. 22 146–22 156, Apr. 2020. [Online]. Available: http://dx.doi.org/10.1021/acsami.0c04097

[40] Q. Zhang and Y. Sun, “Novel metamaterial structures with negative thermal expansion and tunable mechanical properties,” *International Journal of Mechanical Sciences*, vol. 261, p. 108692, Jan. 2024. [Online]. Available: http://dx.doi.org/10.1016/j.ijmecsci.2023.108692

[41] Y. Peng, I. Niloy, M. Kam, P. Celli, and P. Plucinsky, “Programming bistability in geometrically perturbed mechanical metamaterials,” *Physical Review Applied*, vol. 22, no. 1, Jul. 2024. [Online]. Available: http://dx.doi.org/10.1103/PhysRevApplied.22.014073

[42] S. Pyo and K. Park, “Mechanical metamaterials for sensor and actuator applications,” *International Journal of Precision Engineering and Manufacturing-Green Technology*, vol. 11, no. 1, p. 291–320, Aug. 2023. [Online]. Available: http://dx.doi.org/10.1007/s40684-023-00549-w

[43] A. Zolfagharian, P. Picken, M. Bodaghi, M. Fard, and B. Rolfe, “Additive manufacturing of composite foam metamaterial springs for vibration isolation,” *Advanced Engineering Materials*, vol. 25, no. 20, Aug. 2023. [Online]. Available: http://dx.doi.org/10.1002/adem.202300356

[44] F. Pan, Y. Li, Z. Li, J. Yang, B. Liu, and Y. Chen, “3d pixel mechanical metamaterials,” *Advanced Materials*, vol. 31, no. 25, May 2019. [Online]. Available: http://dx.doi.org/10.1002/adma.201900548

[45] A. A., B. B., R. S., and P. V. S., “Sound transmission performance of plate-type acoustic metamaterials for quieter aircraft cabins,” *Applied Acoustics*, vol. 238, p. 110806, Sep. 2025. [Online]. Available: http://dx.doi.org/10.1016/j.apacoust.2025.110806

[46] J. H. Oh, Y. E. Kwon, H. J. Lee, and Y. Y. Kim, “Elastic metamaterials for independent realization of negativity in density and stiffness,” *Scientific Reports*, vol. 6, no. 1, Mar. 2016. [Online]. Available: http://dx.doi.org/10.1038/srep23630

[47] L. Niu, “Optimization design and torque performance research of interior permanent magnet synchronous motors,” *Scientific Reports*, vol. 15, no. 1, Mar. 2025. [Online]. Available: http://dx.doi.org/10.1038/s41598-025-93285-x

[48] H. Ali, M. Adil, and H. Khan, “Digital proportional amplifier of linear dc electromagnet,” *International Journal of Scientific and Engineering Research*, vol. 10, 10 2019.

[49] H. Ge, Y. Miao, B. Bilgin, B. Nahid-Mobarakeh, and A. Emadi, “Speed range extended maximum torque per ampere control for pm drives considering inverter and motor nonlinearities,” *IEEE Transactions on Power Electronics*, vol. 32, no. 9, pp. 7151–7159, 2017.

[50] H. Wang and J. Leng, “Summary on development of permanent magnet synchronous motor,” in *2018 Chinese Control And Decision Conference (CCDC)*. IEEE, Jun. 2018, p. 689–693. [Online]. Available: http://dx.doi.org/10.1109/CCDC.2018.8407219

[51] A. Tessarolo, M. Mezzarobba, and R. Menis, “A new rotor design for flux weakening capability improvement in spoke-type interior permanent magnet synchronous machines,” in *2014 Ninth International Conference on Ecological Vehicles and Renewable Energies (EVER)*. IEEE, Mar. 2014, p. 1–9. [Online]. Available: http://dx.doi.org/10.1109/EVER.2014.6844013

[52] J. Zhao, B. Li, and Z. Gu, “Research on an axial flux pmsm with radially sliding permanent magnets,” *Energies*, vol. 8, no. 3, p. 1663–1684, Feb. 2015. [Online]. Available: http://dx.doi.org/10.3390/en8031663

[53] L. Ma, M. Sanada, S. Morimoto, and Y. Takeda, “Ipmsm with adjustable pm armature flux linkage for high efficiency and wide range operation,” *IEEJ Transactions on Industry Applications*, vol. 121, no. 3, p. 371–376, 2001. [Online]. Available: http://dx.doi.org/10.1541/ieejias.121.371

[54] H. Z. Ruilin, P. and J. X., “Flux linkage regulating and magnetic isolation plate structure for permanent magnet motor rotor,” Jul. 2019.

[Online]. Available: https://permalink.orbit.com/RenderStaticFirstPage?XPN=%252FLQWp3iQXYWG5gAqoCzlqZNXe7dphUsu7KxJINoFg8I%3D%26n%3D1&id=0&base=FULLPAT

[55] J. W. Ambrose, N. Z. R. Chiang, D. S. Y. Cheah, and C.-H. Yeow, "Compact multilayer extension actuators for reconfigurable soft robots," *Soft Robotics*, vol. 10, no. 2, p. 301–313, Apr. 2023. [Online]. Available: http://dx.doi.org/10.1089/soro.2022.0042

[56] A. Simaite, B. Temple, M. Amin Karimi, V. Alizadehyazdi, and M. Spenko, "Understanding the influence of silicone elastomer properties on wedge-shaped microstructured dry adhesives loaded in shear," *Journal of The Royal Society Interface*, vol. 15, no. 146, p. 20180551, Sep. 2018. [Online]. Available: http://dx.doi.org/10.1098/rsif.2018.0551

[57] Smooth-On, Inc., "Smooth-sil 960: Platinum cure silicone rubber," Smooth-On, Inc., Macungie, PA, USA, n.d., accessed: March 18, 2026. [Online]. Available: https://www.smooth-on.com/products/smooth-sil-960/

[58] JSOL Corporation, "Höganäs: Product partners," JMAG International, Tokyo, Japan, n.d., accessed: March 27, 2026. [Online]. Available: https://www.jmag-international.com/aboutus/product-partners/hoganas/

[59] Covestro AG, "Mechanical properties of TPU: Shore hardness and more," Covestro AG, Leverkusen, Germany, n.d., accessed: March 28, 2026. [Online]. Available: https://solutions.covestro.com/ko/highlights/articles/theme/product-technology/mechanical-properties-tpu

[60] ——, "Covestro solution center: Innovative polymer solutions," Covestro Group, Leverkusen, Germany, 2026, accessed: March 28, 2026. [Online]. Available: https://solutions.covestro.com/en

[61] P. Khatake, R. Taluja, M. Sunil Kumar, M. Mahendar Reddy, F. H. Al-Ataby, S. Sood, and P. Sonia, "Cold spray coating: A review of material systems and future perspectives," *Materials Today: Proceedings*, Nov. 2023. [Online]. Available: http://dx.doi.org/10.1016/j.matpr.2023.11.015

[62] L. Gao, H. Zhang, L. Zeng, and R. Pei, "Rotor topology optimization of interior permanent magnet synchronous motor with high-strength silicon steel application," *IEEE Transactions on Magnetics*, vol. 57, no. 2, p. 1–6, Feb. 2021. [Online]. Available: http://dx.doi.org/10.1109/TMAG.2020.3027893

[63] "CA3161790A1 - Methods of manufacturing permanent magnets by additive manufacturing - Google Patents — patents.google.com," https://patents.google.com/patent/CA3161790A1/en?inventor=Jean-Michel+Lamarre&oq=Jean-Michel+Lamarre, [Accessed 30-10-2025].

[64] M. Ibrahim, F. Bernier, and J.-M. Lamarre, "Novel multi-layer design and additive manufacturing fabrication of a high power density and efficiency interior pm motor," in *2020 IEEE Energy Conversion Congress and Exposition (ECCE)*. IEEE, Oct. 2020, p. 3601–3606. [Online]. Available: http://dx.doi.org/10.1109/ECCE44975.2020.9236150

[65] S. Chowdhury, N. Yadaiah, C. Prakash, S. Ramakrishna, S. Dixit, L. R. Gupta, and D. Buddhi, "Laser powder bed fusion: a state-of-the-art review of the technology, materials, properties and defects, and numerical modelling," *Journal of Materials Research and Technology*, vol. 20, p. 2109–2172, Sep. 2022. [Online]. Available: http://dx.doi.org/10.1016/j.jmrt.2022.07.121

[66] D. Goll, F. Trauter, P. Braun, J. Laukart, R. Loeffler, U. Golla-Schindler, and G. Schneider, "Additive manufacturing of permanent magnets based on (cocufezr)17sm2," *physica status solidi (RRL) - Rapid Research Letters*, vol. 15, no. 10, Aug. 2021. [Online]. Available: http://dx.doi.org/10.1002/pssr.202100294

[67] B. Liu, Y. Wang, Z. Lin, and T. Zhang, "Creating metal parts by fused deposition modeling and sintering," *Materials Letters*, vol. 263, p. 127252, Mar. 2020. [Online]. Available: http://dx.doi.org/10.1016/j.matlet.2019.127252

[68] C. Miguel-Espinar, D. Heredero-Peris, R. Villafafila-Robles, and D. Montesinos-Miracle, "Review of flux-weakening algorithms to extend the speed range in electric vehicle applications with permanent magnet synchronous machines," *IEEE Access*, vol. 11, p. 22961–22981, 2023. [Online]. Available: http://dx.doi.org/10.1109/ACCESS.2023.3252360